Petroleum Science 23 (2026) 1728–1753

Contents lists available at ScienceDirect

Petroleum Science

journal homepage: www.keaipublishing.com/en/journals/petroleum-science

Original Paper

Effects of lamina on petrophysical properties and brittleness of shales: Insight from lamina-scale experiment and fracture propagation simulation

Yu-Qi Wu [a,b,c,d], Jia-Bao Yang [a,d], Ke-Yu Liu [a,d,*], Chao-Zheng Deng [a,d], Yu-Chen Fan [e,]

[f] School of Energy Science and Engineering, Henan Polytechnic University, Jiaozuo, 454000, Henan, China
[g] PetroChina Dagang Oilfield Exploration and Development Research Institute, Tianjin, 300280, China

ARTICLE INFO

Article history:
Received 6 August 2025
Received in revised form
9 October 2025
Accepted 21 January 2026
Available online 25 January 2026

Edited by Xi Zhang and Jie Hao

Keywords:
Shale lamina
Lamina-scale characterization
Brittleness
Shale oil development

ABSTRACT

Accurate shale characterization is hampered by the lack of high-resolution analytical techniques to probe the in situ petrophysical and mechanical properties at the lamina scale. Here we report for the first time a comprehensive lamina-scale experimental characterization and numerical simulation, including AMICS, digital rock, fracture propagation simulation, pore network modeling, FIB-SEM, and N_2 and CO_2 adsorption experiments to investigate the effects of lamina type and thickness on the petrophysical properties and brittleness of shales. We characterized a variety of shales with laminae dominated by felsic minerals, carbonate minerals, clay minerals, and mixed minerals from the Second Member of the Kongdian Formation in the Cangdong Sag, Bohai Bay Basin. Among these laminae investigated, the felsic mineral lamina exhibits the largest porosity, average macropore radius, pore throat radius, and coordination number, and the best pore connectivity and permeability. The carbonate mineral lamina comprises the largest proportion of micropores and the smallest proportion of macropores. The mixed mineral lamina consists mainly of mesopores and micropores. Shales in the study area mainly comprise felsic-mineral-clay-mineral, carbonate-mineral-clay-mineral, and mixed-mineral-clay-mineral coupled laminasets. The felsic-mineral-clay-mineral laminaset appears to have the best permeability and brittleness. The simulated fractures in the felsic-mineral-clay-mineral laminaset show the farthest propagation and the largest aperture. An increase in the thickness of individual felsic mineral lamina would improve the shale brittleness, increase fracture propagation, and enhance fracture connectivity. Fractures tend to be initiated at the interface between the clay mineral lamina and brittle mineral lamina, especially at the boundaries between the ductile and brittle minerals. Therefore, shales with high proportions of felsic mineral lamina would thus improve the porosity, permeability, and frackability of shales. This study proposes a novel technique for characterizing the in situ petrophysical properties and brittleness of shales at the lamina scale.

1. Introduction

Shales are heterogeneous since they are composed of extremely thin laminae, most of which are micrometers (Fan et al., 2022; Loucks et al., 2021; McMahon et al., 2024; Reed et al., 2019). Different laminae consist of various minerals and pores. Lamina

* Corresponding author.
** Corresponding author.
E-mail addresses: liukeyu@upc.edu.cn (K.-Y. Liu), fanyuchen614@163.com (Y.-C. Fan).
Peer review under the responsibility of China University of Petroleum (Beijing).

https://doi.org/10.1016/j.petsci.2026.01.038

structures control the petrophysical properties and brittleness of shales (Loucks and Ruppel, 2007; Zhang et al., 2018; Zhao et al., 2020a). However, the accurate characterization of the effects of lamina type and thickness on shale properties is hindered by the lack of high-resolution analytical and experimental techniques to probe the in situ petrophysical properties and brittleness at the lamina scale, as current experimental instruments are designed for centimeter-scale samples. Thus, this study presents a novel technique combining multiple experimental and numerical methods to characterize the shale properties at the lamina scale.

A lamina is the smallest megascopic layer in a sedimentary sequence and is relatively uniform in composition and texture (Campbell, 1967; Reed et al., 2019). Each kind of lamina forms under essentially constant physical conditions of deposition, and each can be considered a sedimentation unit. A laminaset is made of two or more conformable laminae (Campbell, 1967). In sedimentology, each group of laminae representing a ripple is a laminaset. Currently, laminated shale is considered a favorable and promising lithofacies for shale oil (Cao et al., 2024; Jin, X. et al., 2021; Jin, Z. et al., 2021), e.g., the organic-rich siliceous laminated shale of the Chang 7_3 sub-member in the Ordos Basin, China (Xi et al., 2020), and the organic-rich laminated shale of the Shahejie Formation in the Jiyang Depression of the Bohai Bay Basin, China (Liang et al., 2023). Notwithstanding, terrestrial shale is highly heterogeneous and has diverse laminasets and variable geometric properties. The petrophysical properties and brittleness of shale reservoirs with different laminasets vary greatly, and their main controlling factors remain unclear. Thus, it is a great difficulty to predict how the physical properties of the shales with different laminae change, so the prediction of the sweet spots of shale oil is sometimes not accurate, and the reservoirs with different laminae show unstable production capabilities (Han et al., 2021; Jin, X. et al., 2021). Therefore, it is necessary to figure out the controlling effects of laminae on the physical properties and frackability of shale reservoirs to promote efficient shale oil development (Jin, X. et al., 2021; Jin, Z. et al., 2021; Nath and Mokhtari, 2018).

Laminae are the result of the deposition of sediments with different minerals (Campbell, 1967; Schieber, 1990). Most shales worldwide contain lamina structures. Loucks and Ruppel (2007) found that there are plenty of laminated lime mudstones in Forestburg limestone, Fort Worth Basin, Texas. In laminated mudstones, the percentages of carbonate and clay minerals are different (Loucks and Ruppel, 2007). Also, the organic-matter-rich, clast-rich, and styliolinid-rich laminae were identified in the Marcellus Shale (Bruner et al., 2015). Later, Liu et al. (2019) found that shales in the Cretaceous Qingshankou Formation in the Gulong Sag, Songliao Basin, China consist of laminated argillaceous, laminated siliceous mudstone, bedded siliceous siltstones, and bedded calcareous mudstones (Liu et al., 2019). Recently, Zhao et al. (2024) revealed that the lamina type, mineral content, and thermal maturation have a great effect on the petrophysical properties and brittleness of shales (Zhao et al., 2024). Ma et al. (2024) and Zhang et al. (2025) investigated the mechanical properties and brittleness of heterogeneous shales by using the microindentation and finite element methods, respectively (Ma et al., 2024; Zhang et al., 2025).

Due to the difference in the minerals, different laminae have distinct effects on the pore structures, permeability, and elastic properties among the rocks (Iqbal et al., 2021; Xu et al., 2020; Zhang et al., 2018). Some scholars have investigated the impact of lamina types, development frequency, thickness, continuity, and dip angle on the petrophysical and mechanical properties, frackability, oil movability, and oil content of shale reservoirs, exhibited in Fig. 1 (Allan et al., 2015; Ghanizadeh et al., 2014; Jin, X. et al., 2021; Nath and Mokhtari, 2018; Shi et al., 2018; Wang et al., 2019). For example, the rock physics team at Stanford University revealed that the smaller the dip angle of the laminations or the better the continuity of the clay laminations in the shale, the smaller the shale's elastic modulus (Allan et al., 2015; Vernik and Nur, 1992). Jin, X. et al. (2021) figured out that the development frequency of laminations controls the horizontal permeability of shale, thereby affecting the lateral migration and development effectiveness of shale oil. Xi et al. (2020) discovered that in the Chang 7_3 submember of the Ordos Basin, China, the organic-rich siliceous laminated shale has more developed dissolved pores, and its reservoir quality is better than that of the organic-rich tuffaceous laminated shale. Loucks et al. (2021) found that the rocks in the Upper Cretaceous Austin Chalk Group, USA, contain multiple types of laminae, from poorly, moderately to well-laminated chalk, and the total organic carbon of different laminae is different. As a result, the lamina structure greatly affects the petrophysical properties and brittleness of shales. Although these studies focus on single or fewer influencing factors, they often remain at the level of phenomenological characterization. There is a lack of systematic and in-depth research on the effects of lamina types on shale porosity, permeability, and brittleness, which limits the evaluation and efficient development of shale oil sweet spots.

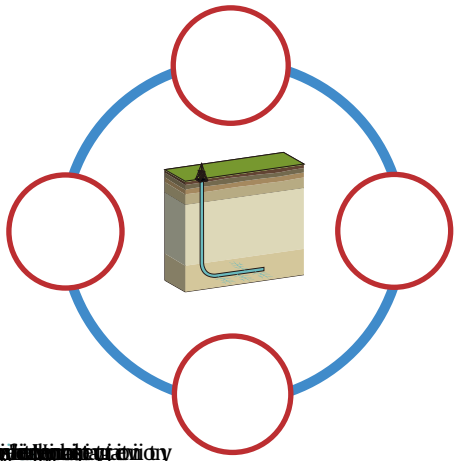

Fig. 1. Effects of lamina structure on petrophysical properties, frackability, oil mobility, and oil content of shale reservoir.

Currently, the widely used methods for investigating the impact of laminae on shale rock petrophysical properties and brittleness are two-dimensional mineral analysis techniques and rock physics experiments (Xu et al., 2024). Two-dimensional mineral analysis techniques, for example, Scanning Electron Microscopy (SEM) with Energy Dispersive X-ray Spectroscopy (EDS), can be used to reveal the differences in microstructural composition between various lamina groups at the micro- and nanoscale, but they cannot simultaneously measure shale permeability and brittleness. Rock physics experiments can be used to determine the porosity, permeability, and brittleness of core samples at the centimeter scale, but due to the extremely thin laminae in shales, the diversity in lamina types, and variable geometric properties, there are significant differences in lamina types, development frequencies, thicknesses, and continuity between different rock samples. This makes it difficult to establish a clear relationship between experimental results and lamination types or geometric properties. Therefore, some numerical methods should be combined with the experiments to overcome these research challenges. The digital rock technique, as an effective numerical

Different from the classic pore network models, considering the effect of slip in a shale reservoir, the fluid is usually classified as the adsorption phase near solid grains and the bulk phase in the center of the pores. The flow capacity of a cylinder, saturated by shale oil, is a function of pore structure, slip length, the thickness of the adsorption phase, as well as viscosity ratio, and the density ratio of the two phases (Song et al., 2021). The conductance of a cylinder is calculated based on Eq. (2).

$$k_{ij} = \frac{A}{\mu_b L}\left[\underbrace{\frac{(R-t_a)^4}{8R^2} + \frac{\mu_b}{\mu_a}\frac{2Rt_a - t_a^2 + 2L_sR}{4R^2}(R-t_a)^2}_{\text{Adsorption phase}} + \underbrace{\frac{\mu_b}{\mu_a}\frac{\rho_a}{\rho_b}\frac{2\left(R^2+2L_sR\right)\left(2Rt_a-t_a^2\right)-\left(R^4-(R-t_a)^4\right)}{8R^2}}_{\text{Bulk phase}}\right] \tag{2}$$

where A represents the cross-sectional area of the throat. R signifies the radius of the throat. t_a is the thickness of the adsorption phase, assuming 0.7 nm in this work. The subscripts a and b represent the adsorption phase and bulk phase, respectively. μ is the viscosity of the fluid, $\mu_b/\mu_a = 0.5$. ρ represents the density, $\rho_b/\rho_a = 0.5$. L is the length of the throat. Octane is utilized to represent the shale oil in this work, and the slip length (L_s) of octane is calculated by the following equation (Song et al., 2021):

$$L_s = 10^{-9}\times\left[8.4474e^{\left(\frac{N_A}{7.1517\times10^{31}}\frac{dp}{dx}\right)} - 2.3316 \times 10^{-5}e^{\left(\frac{T}{30.1824}\right)} + 330.7129e^{\left(\frac{\times10^9}{-0.9702}\right)} + 87.3782\right] \tag{3}$$

where $N_A = 6.022\times10^{23}$ is the Avogadro constant. is the width of the throat section. T is the temperature of the fluid, being 400 K in the calculation.

2.5. Fracture propagation simulation and brittleness index

In this study, a finite-element-based software, Rock Failure Process Analysis 3D (RFPA3D), is used to simulate fracture propagation and evolution of different shale laminasets. Through the weakening and strengthening of elements, it simulates the deformation and failure processes within rocks, making it possible to model the entire process of rock behavior from microscopic damage to macroscopic failure (Tang and Zhao, 1997). RFPA3D has been widely used to simulate the compression and fracturing processes of rocks such as shale, sandstone, and granite (Dong et al., 2024; Liu et al., 2022, 2023; Meng et al., 2023).

The simulation of this software is based on several fundamental assumptions. First, rock failure occurs when its deformation reaches a certain threshold. Also, failed elements have no tensile strength but retain some compressive strength. The heterogeneity of rocks can be represented by the heterogeneous assignment of rock mechanical parameters. The changes in the mechanical properties of failed elements are irreversible (Tang et al., 1999). By introducing distribution functions (such as the Weibull distribution, the uniform distribution, and the normal distribution), it assigns heterogeneous properties to microscopic elements to simulate the macroscopic nonlinearity of rocks. The Weibull Distribution is used in this simulation as the following equation:

$$f(u) = \frac{m}{u_0}\times\left(\frac{u}{u_0}\right)^{m-1}\times e^{\left(-\frac{u}{u_0}\right)^m} \tag{4}$$

where u represents the mechanical parameter (such as elastic modulus) of elements. u_0 signifies the average value of the mechanical parameter of the elements. m is the shape parameter of the Weibull distribution, which characterizes the heterogeneity of elements. Elements become more homogeneous as the value of m increases.

When the element is in a tensile state, its failure criterion is shown as follows:

$$\varepsilon_3 \le \frac{\sigma_{t0}}{E} \tag{5}$$

where E represents the elastic moduli of the damaged elements. ε_3 signifies the minimum principal strain. σ_{t0} is the uniaxial tensile strength. The Mohr-Coulomb criterion is applied to cases where an element undergoes shear failure. In rock mechanics, failure occurs when the shear stress on a certain plane within the rock exceeds its shear strength. The Mohr-Coulomb failure criterion is defined as follows:

$$F = \sigma_1 - \sigma_3\frac{1+\sin\varphi}{1-\sin\varphi} \ge \sigma_{c0} \tag{6}$$

where σ_1 and σ_3 represent the maximum and minimum principal stresses, respectively. σ_{c0} denotes the uniaxial compressive strength. φ signifies the internal friction angle of the element, reflecting the frictional resistance between elements. RFPA3D adopts the Mohr-Coulomb failure criterion with tensile cut-off. The tensile strain criterion is given priority in determining whether an element fails. If the element does not reach tensile failure, the Mohr-Coulomb criterion is then used to assess whether the element fails. In elastic damage mechanics, the stiffness of an element gradually decreases as damage progresses (Zhu and Tang, 2004). The relationship between the Young's modulus before and after element damage is shown in Eq. (7):

$$E = (1-D)E_0 \tag{7}$$

where E_0 denotes the Young's modulus of undamaged elements. D represents the damage variable ($0 < D < 1$). $D = 0$ indicates no damage to the element, $D = 1$ reveals complete damage to the element (Liu et al., 2022).

Under tensile conditions, the expression for the mesoscopic element damage variable is shown in Eq. (8):

$$D = \begin{cases} 0 & \varepsilon_{t0} \le \varepsilon < 0 \\ 1 - \dfrac{\lambda \varepsilon_{t0}}{\varepsilon} & \varepsilon_{tu} \le \varepsilon < \varepsilon_{t0} \\ 1 & \varepsilon \le \varepsilon_{tu} \end{cases} \tag{8}$$

where ε is the strain. λ represents the residual strength coefficient. ε_{t0} denotes the strain at peak tensile stress, which serves as the tensile damage strain threshold. ε_{tu} signifies the ultimate tensile strain of the element. When this limit is reached, $D = 1$, the element is completely damaged, and its mechanical parameters are nearly zero. At this point, the Young's modulus of the element is replaced with a very small number, such as 1.0×10^{-5}.

Under compressive stress conditions, the expression for the damage variable of a rock element is shown in Eq. (9):

$$D = \begin{cases} 0 & 0 \le \varepsilon < \varepsilon_{c0} \\ 1 - \dfrac{\lambda \varepsilon_{c0}}{\varepsilon} & \varepsilon_{c0} \le \varepsilon \end{cases} \tag{9}$$

where ε_{c0} denotes the strain at the peak compressive stress. The failure evolution mode of the element is shown in Fig. 2.

Shale brittleness can be computed based on the Rickman model, which is a widely used approach for evaluating materials' brittleness based on Young's modulus and Poisson's ratio (Lai et al., 2016; Rickman et al., 2008; Zhang et al., 2025). It calculates the Brittleness Index (BI) by comprehensively considering both Young's modulus and Poisson's ratio (Rickman et al., 2008). The calculation method for the Brittleness Index BI is shown in Eqs. (10)–(12):

$$\mathrm{BI}_E = \frac{E - E_{\min}}{E_{\max} - E_{\min}} \tag{10}$$

$$\mathrm{BI}_\nu = \frac{\nu - \nu_{\max}}{\nu_{\min} - \nu_{\max}} \tag{11}$$

$$\mathrm{BI} = \frac{\mathrm{BI}_E + \mathrm{BI}_\nu}{2} \times 100\% \tag{12}$$

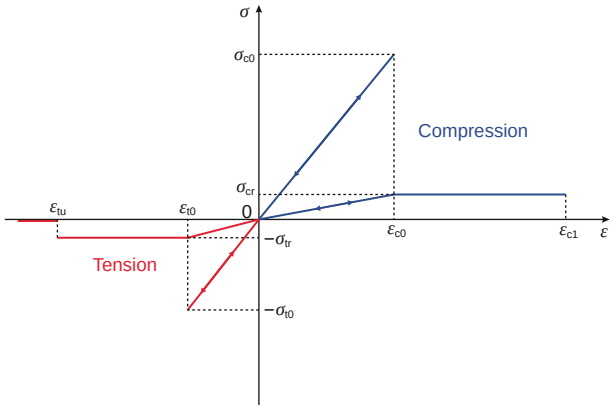

Fig. 2. Elastic-brittle damage constitutive law of elements.

where E represents Young's modulus and ν signifies Poisson's ratio. The subscripts max and min represent the maximum and minimum values of these parameters within the calculated models, respectively. BI_E and BI_ν represent the brittleness indices calculated based on Young's modulus and Poisson's ratio, respectively.

3. Geological background

The studied shale samples are from the Second Member of Kongdian Formation of the Cangdong Sag in the Bohai Bay Basin, China. The Cangdong Sag is a secondary tectonic unit in the Huanghua Depression of the Bohai Bay Basin (Fig. 3). It was formed by regional tension based on an early depression-type lake basin, adjacent to the Xuhei Uplift, Cangxian Uplift, Dongguang Uplift, and Kongdian Uplift. It is a Cenozoic intracontinental faulted lake basin with an area of approximately 1760 km^2. The Cangdong Depression is located between the Xuxi Fault and the Cangdong Fault, presenting a structural pattern of two depressions with one uplift (Xin et al., 2022; Zhao et al., 2020b). The Cangdong Sag has deposited the Kongdian Formation, Shahejie Formation, Dongying Formation, Guantao Formation, Minghuazhen Formation, and Pingyuan Formation from bottom to top since the Paleogene. The Kongdian Formation is the earliest formation developed in the Huanghua Depression during the Cenozoic era, with a total thickness of 2500 m, and is in angular unconformable contact with both sets of strata.

During the deposition of the second member of the Kongdian Formation, lacustrine dark gray fine-grained sedimentary rocks were deposited in the center of the study area, with a large coverage area and a wide extension range. A lacustrine deposition system was developed with sediments from the northeast, northwest, and southwest directions, comprising semi-deep to deep lacustrine, braided river delta, fan delta, and meandering river delta deposits. The Kongdian Formation develops from bottom to top into the Third Member (Ek_3), Second Member (Ek_2) and First Member (Ek_1). In terms of rock formation color, there is a characteristic of "red-black-red" variation from bottom to top. There is a pattern of "coarse-fine-coarse" in terms of granularity. The Second Member of the Cangdong Sag is a complete third-order sequence (Ek_2), which is the largest lacustrine deposition of the Kongdian Formation. The thickness of the black shale exceeds 400 m. The Second Member of the Cangdong Sag can be divided into four submembers (Ek_2^4, Ek_2^3, Ek_2^2, Ek_2^1). Ek_2^4 is mainly composed of delta sediments and consists of gray fine sandstone and gray mudstone. Ek_2^3 and Ek_2^2 represent the deep and semi-deep lacustrine deposits. The rocks include black shales and siltstones, with a thickness from 100 to 300 m. The formation of Ek_2^1 is composed of black shales and dolomite (Xin et al., 2022). The vitrinite reflectance values of the Second Member of the Cangdong Sag, which range between 0.66% and 0.91%, indicate that the shales are at a low to moderate maturity stage (Zhao et al., 2019).

The shales in the Second Member of the Cangdong Sag are heterogeneous and composed of various laminae. As shown in Fig. 4, fluorescence scanning, general optical scanning, and optical microscopy reveal that the laminae of shales of this formation comprise felsic mineral, carbonate mineral, clay mineral, and mixed mineral laminae (Zhao et al., 2020a). There is a significant difference in the thickness of the laminae, ranging from 10 μm to 2 mm. The occurrence frequency of laminae is from 2 to 40 laminae per millimeter. The laminae are mostly distributed in a plate-like pattern, with a visible wavy distribution. Both continuous and intermittent laminae exist.

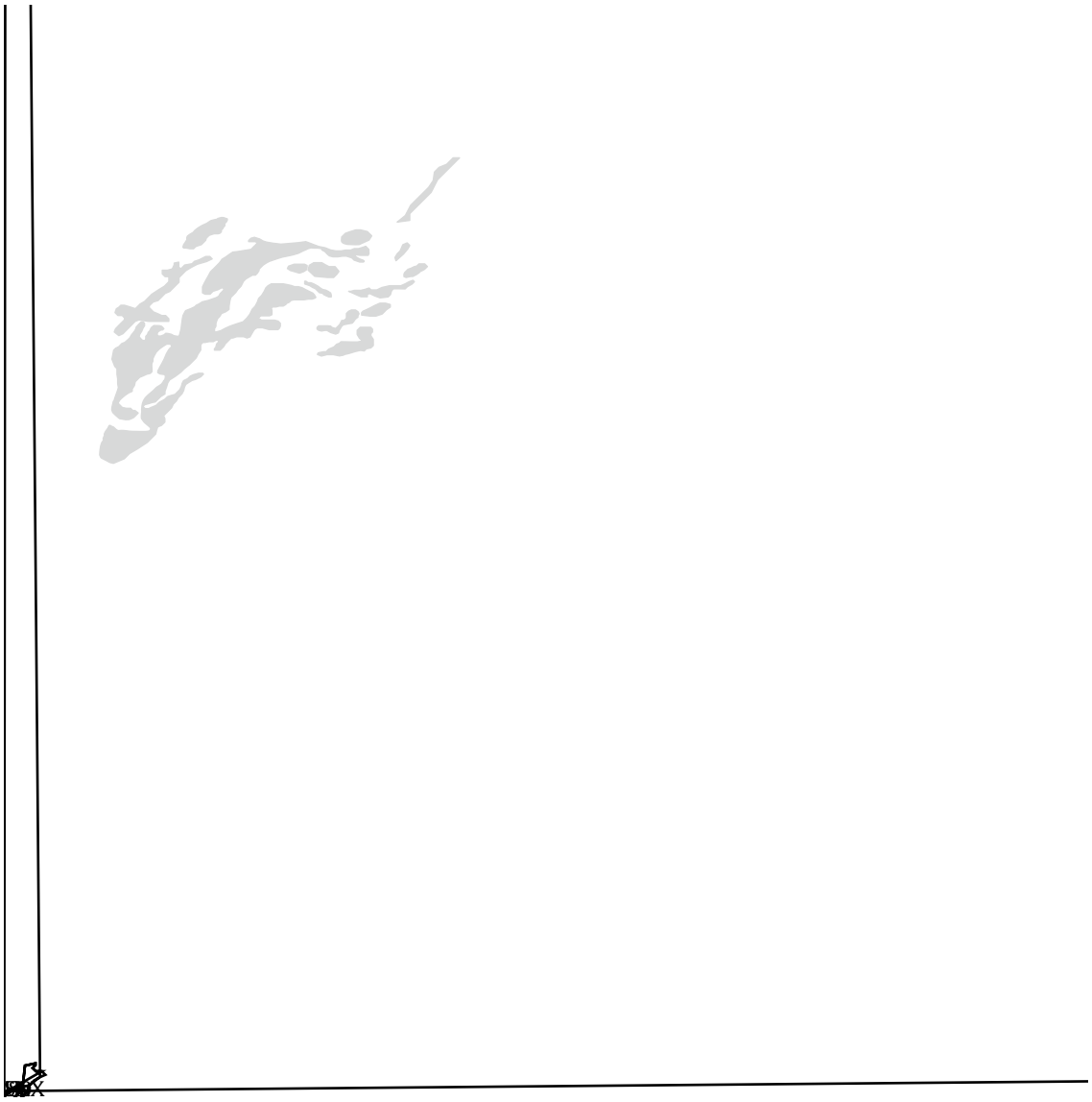

Fig. 3. Location and structural map of the Cangdong Sag in the Bohai Bay Basin, China.

4. Results and discussion

4.1. Lamina-scale experimental characterization

4.1.1. Lamina type

The shale reservoir of the Second Member of Kongdian Formation in Cangdong Sag of Bohai Bay Basin has the characteristics of high-frequency lamina laminations (more than 10,000 laminae/m). The fine-grained sedimentary rocks in this formation have complex layer types, diverse combination styles, frequent interaction of layers, and variable geometric properties. The definition of lamina depends on the content of felsic minerals, clay minerals, and carbonate minerals within this lamina. Through observation and analysis of hundreds of SEM images, it is found that the shales in the study area mainly include the felsic mineral lamina, carbonate mineral lamina, clay mineral lamina, and mixed mineral lamina exhibited in Figs. 5 and 6. Compared to the former four laminae, there are a few analcite mineral laminae. Felsic minerals and clay minerals are mainly from terrestrial detrital sources. Felsic minerals represent mechanical sedimentation, clay minerals represent colloidal sedimentation, and carbonate minerals mainly precipitate in the basin, representing chemical sedimentation. Organic matter represents biological sedimentation. The coexistence of multiple types of laminae indicates that the fine-grained sedimentary rocks in the Second Member of Kongdian Formation have mixed deposition characteristics, which are jointly controlled by mechanical sedimentation, chemical sedimentation, and biological sedimentation.

When felsic minerals (e.g., quartz and feldspar) are enriched in a certain layer and their content exceeds 50% of all materials in this layer, the layer is called the felsic mineral lamina. Under the microscope, it is observed that this kind of lamina appears gray and grayish white, wherein large quartz and feldspar particles are visible, as shown in Fig. 4. Clay minerals and a small amount of organic matter fill the feldspar mineral particles. The kinds of clay minerals are illite and chlorite. The interface of this lamina is clear and visible, with good continuity and a flat overall seam surface. The total content of feldspar and quartz in the felsic mineral lamina is about 57%, clay minerals approximately occupy 21%, and the content of dolomite and calcite is relatively low, about 15%, as

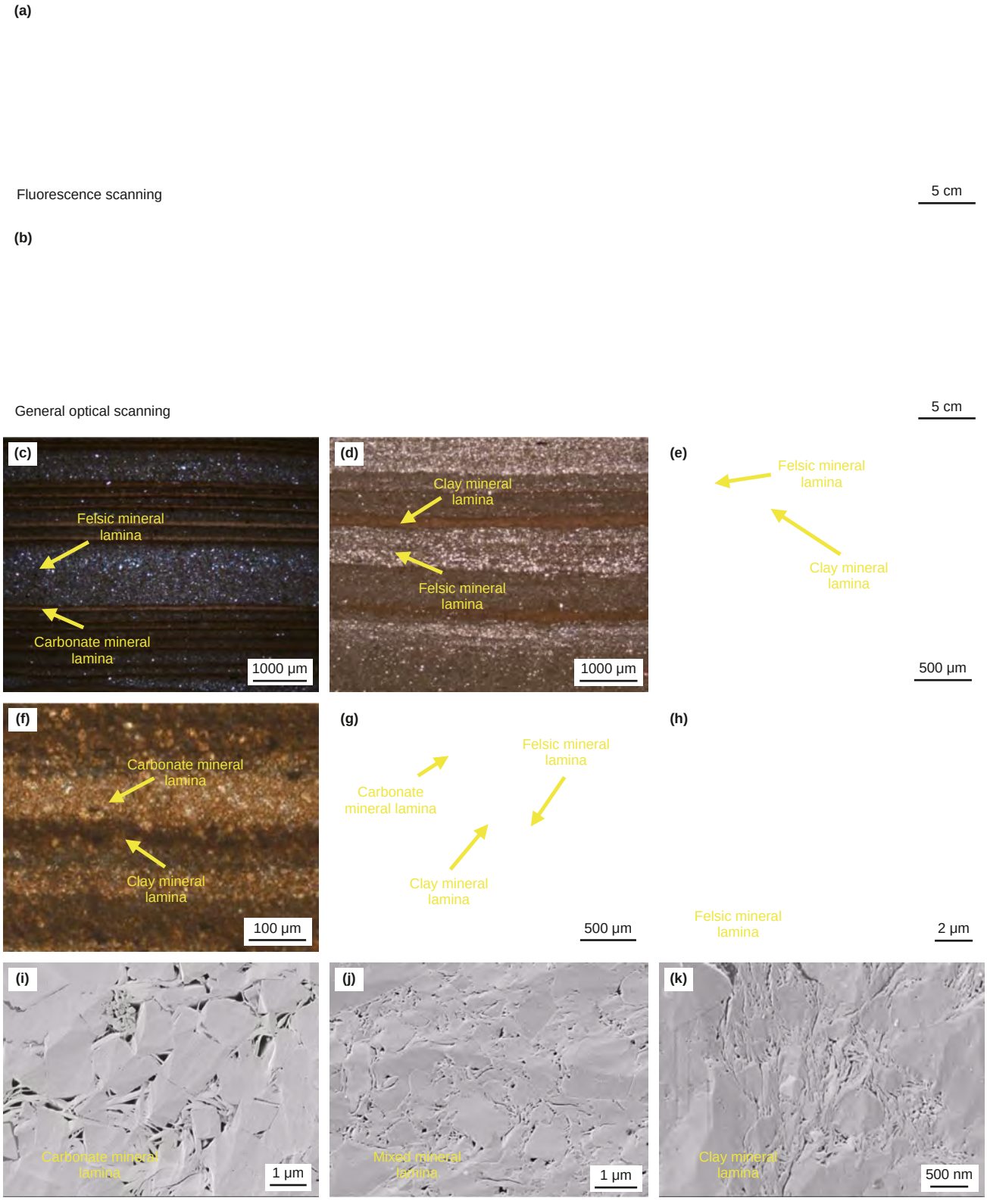

Fig. 4. Laminae and laminasets in the shales of Kongdian Formation of the Cangdong Sag in the Bohai Bay Basin, China. **(a)** Fluorescence scanning and **(b)** general optical scanning of laminated shale, 3224.5 m, G108-8 well (modified from Zhao et al., 2020a). **(c)** Felsic mineral and carbonate mineral laminae, 3330.66 m, G108-8 well. **(d)** Clay and felsic mineral laminae, 3341.65 m, G108-8 well. **(e)** Felsic mineral and clay mineral laminae, 2986.65 m, G108-8 well. **(f)** Carbonate mineral and clay mineral laminae, 3231.25.66 m, G108-8 well. **(g)** Felsic mineral, carbonate mineral, and clay mineral laminae, 2986.25 m, G108-8 well. **(h)** Felsic mineral lamina, 3280.87 m, G108-8 well. **(i)** Carbonate mineral lamina, 3130.97 m, G108-8 well. **(j)** Mixed mineral lamina, 2981.93 m, G108-8 well. **(k)** Clay mineral lamina, 3049.11 m, G108-8 well.

Fig. 5. Various laminae and laminasets of shales. The height and width of these images are 1.1 mm and 110 μm, respectively. **(a)–(b)** SEM and AMICS images, 3233.07 m, G108-8 well. **(c)–(d)** SEM and AMICS images, 3248.06 m, G108-8 well. AMICS image, 3248.06 m, G108-8 well. **(e)–(f)** SEM and AMICS images, 3248.04 m, G108-8 well (modified from Fan, 2023).

exhibited in Fig. 7. The percentage of organic matter is high, with an average TOC value of about 4.37%. The diameter of feldspar particles varies greatly, ranging from 2 to 70 μm, with an average of 23 μm. The thickness of the felsic mineral lamina varies, ranging from 12 to 187 μm. When carbonate minerals (calcite and dolomite) are enriched in layers and their content exceeds 50% of all components in this layer, the layer is called the carbonate mineral lamina. Under the microscope and scanning electron microscope, the carbonate mineral lamina appears gray-brown and brown, as displayed in Figs. 4 and 7. This type of lamina is composed of dolomite and calcite, with a total content of about 63%. The average clay mineral content is about 18%, and the average feldspar content is roughly 16%. AMICS results show that the area proportion of organic matter can reach 6%, with an average of approximately 3.62%. The diameter of dolomite and calcite particles ranges from 1 to 36 μm, with an average diameter of 21 μm. The diameter range of quartz and feldspar particles varies from 3 to 32 μm. The thickness of the carbonate mineral lamina varies greatly, ranging from 25 to 134 μm.

When the proportion of clay minerals in a specific layer exceeds 50%, the layer can be referred to as a clay mineral lamina. Clay minerals mainly include illite and chlorite. When clay minerals are continuously distributed in strip patterns, feldspar, quartz, and dolomite particles in the layers are dispersed within those clay minerals. The thickness of individual layers ranges from 14 to 163 μm. The area percentage of the organic matter is different in such lamina, changing from 0.2% to 15.6%, with an average of about 5.22%. Organic matters are in a continuous, elongated distribution. When felsic minerals and carbonate minerals (calcite and dolomite) are mixed and the mineral content of a certain type does not exceed 50%, the layer is categorized as a mixed mineral lamina. The main minerals in the mixed mineral lamina include albite, K-feldspar, calcite, quartz, dolomite, illite, and chlorite, which are evenly distributed in the lamina. The average TOC value ii T09 w T01, K

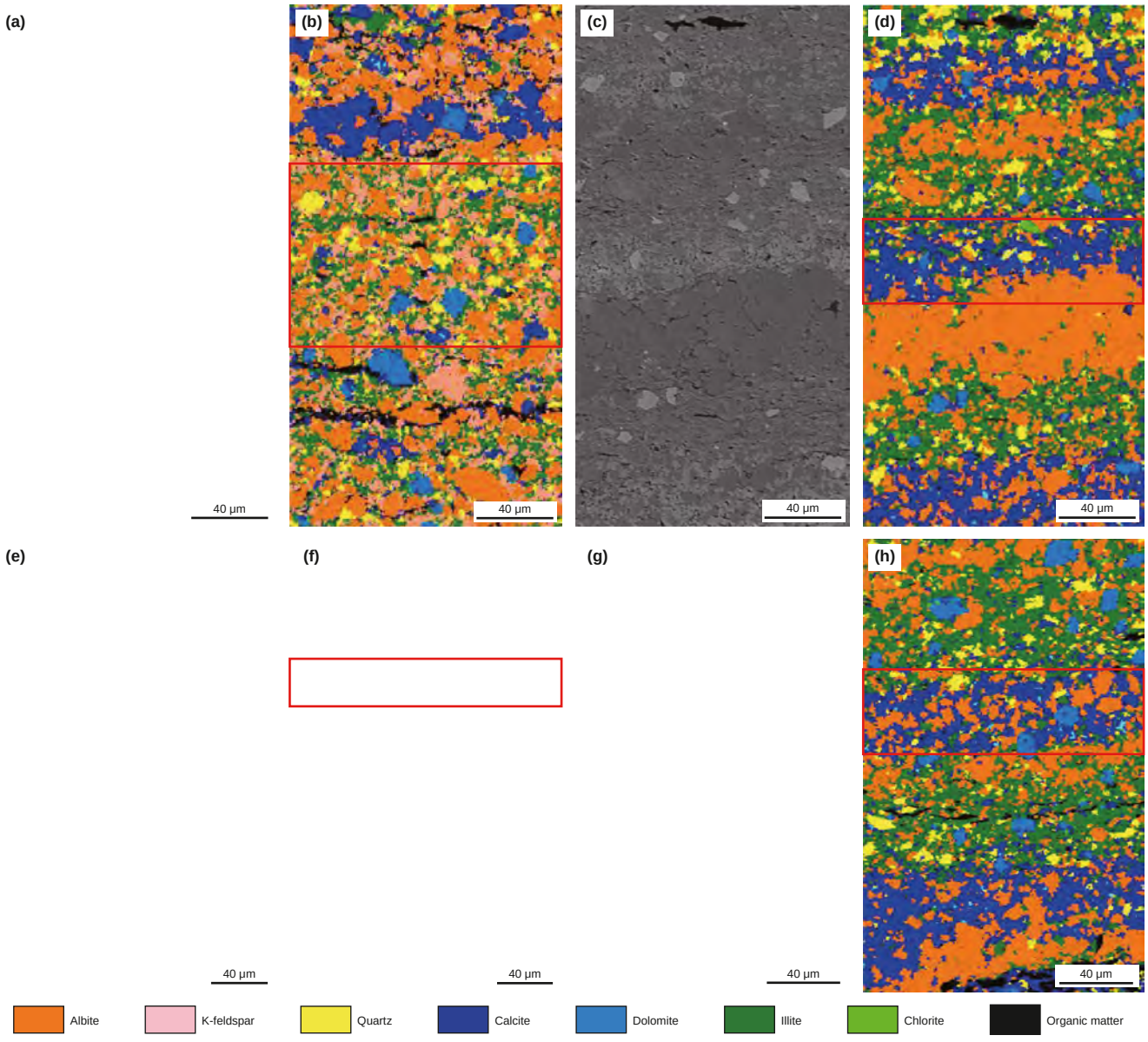

Fig. 7. Lamina types of the shales in the Second Member of Kongdian Formation of Cangdong Sag, Bohai Bay Basin, which are highlighted in the red boxes.

particles are slightly larger, with diameters ranging from 2 to 43 μm. The thickness of the layer also varies, ranging from 26 to 68 μm.

4.1.2. Laminaset type

Different types of laminae are vertically stacked to form different styles of laminasets. Based on identifying the lamina types in the Second Member of Kongdian Formation of the Cangdong Sag, the common laminasets are determined. The felsic-mineral-clay-mineral, carbonate-mineral-clay-mineral, and mixed-mineral-clay-mineral laminasets widely exist in this formation. Also, there are a few felsic-mineral-carbonate-mineral, carbonate-mineral-mixed-mineral, and felsic-mineral-mixed-mineral laminasets. Apart from the combinations of two laminae, the combinations of three laminae, such as the felsic mineral lamina, the clay mineral lamina, and the carbonate mineral lamina, also exist in the formation. Considering the occurrence frequency of these laminae, we focus on the characteristics of felsic-mineral-clay-mineral, carbonate-mineral-clay-mineral, and mixed-mineral-clay-mineral laminasets and their effects on the petrophysical properties and brittleness. The thickness of these laminae varies greatly, ranging from 5 μm to 2 mm. The occurrence frequency of laminasets varies greatly among samples of different depths, ranging from 1 to 50 laminae per millimeter.

The laminasets are mostly distributed in a plate-like parallel pattern, with both continuous and intermittent distribution. For the felsic-mineral-clay-mineral laminaset, its occurrence frequency is quite high in Ek_2, the thickness of the two types of laminae varies and is up to 163 μm. The content of illite and chlorite is relatively high in the clay mineral lamina, and the clay mineral content in some laminae can exceed 85%. Felsic mineral and clay mineral laminae are mostly distributed in a continuous parallel manner. The carbonate-mineral-clay-mineral laminaset occurs quite frequently, usually accompanied by the felsic mineral

lamina. The thickness of clay mineral lamina is greater than that of the carbonate mineral lamina, with the former ranging from 23 to 152 μm while the latter ranging from 17 to 138 μm. Both laminae are mostly distributed in a continuous and parallel manner.

The mixed-mineral-carbonate-mineral laminaset generally has a low occurrence frequency. Its thickness is usually less than 100 μm, smaller than that of the clay mineral lamina. Albite and calcite are the main minerals in the mixed mineral lamina, while illite is the most abundant mineral in the clay mineral lamina. The felsic minerals in these laminasets are typical of terrestrial detrital minerals, representing mechanical sedimentation, while the carbonate minerals are mainly basin minerals, representing chemical sedimentation. tiol treX6500AzJHthicX51AwJHknes1q X6zA1JHoq1X6500AzJHthe X6kT@J Hfelsi6k5q X65AzJHmineral X6zzA.JHlami 1qz XqA.JHi

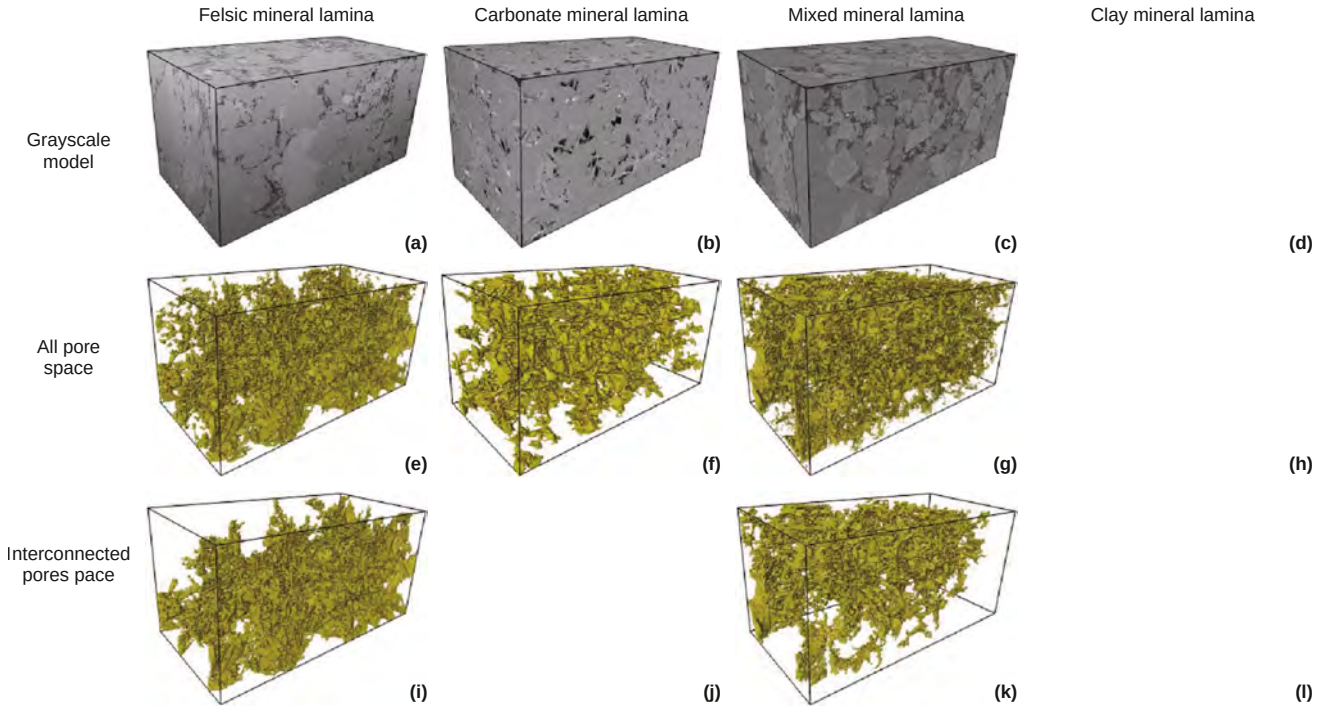

Fig. 9. Digital models, all pore space, and connected pore space of four kinds of laminae. **(a)**, **(e)** and **(i)** Felsic mineral lamina, 4105.68 m, GD14 well. **(b)**, **(f)**, and **(j)** Carbonate mineral lamina, 4087.15 m, G108-8 well. **(c)**, **(g)**, and **(k)** Mixed mineral lamina, 3856.00 m, GD12 well. **(d)**, **(h)**, and **(l)** Clay mineral lamina, 3049.11 m, G108-8 well. The resolution and dimension of the models are 30 nm and 2800 × 1400 × 1400 voxels, respectively.

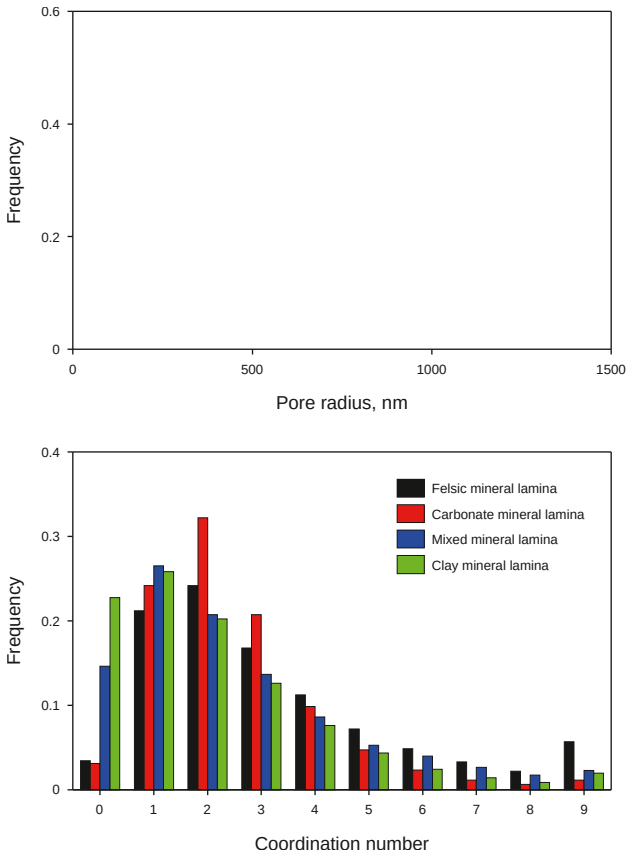

Fig. 10. Pore radius distribution, throat radius distribution, coordination number distribution, and multiple-point correlation function (MPCF) of four kinds of laminae. The MPCF indicates the pore connectivity.

good, larger than 70%. The porosity of the clay mineral lamina is 3.31% and smallest among all the laminae. Although the pores in this lamina are evenly distributed in the model, the distribution of the connected pores is extremely heterogeneous and only occupies a small region of the whole pore system.

Apart from the qualitative analysis, the pore radius distribution, throat radius distribution, coordination number distribution, and multiple-point correlation function of four kinds of laminae are computed and quantitatively compared, displayed in Fig. 10. It is obvious that the pore-system characteristics of the laminae are different. The average pore and throat radii of the felsic mineral lamina are the largest among all the kinds of laminae, which are 273.79 nm and 155.00 nm, respectively. The pore radius distribution of the carbonate mineral lamina is bimodal, which involves multiscale pores from 45 to 1200 nm. The average pore and throat radii of this kind of lamina are 231.02 nm and 87.18 nm, respectively. By comparison, the aperture of the clay mineral lamina is the smallest among those laminae. The average pore and throat radii of the clay mineral lamina are 89.71 nm and 31.31 nm, respectively. Three-dimensional pore-system distributions of these laminae exhibited in Fig. 9, reveal such differences in the aperture of the laminae. The multiple-point correlation function of the pore space represents the probability of the multiple voxels in the model all being in the pore space. The high probability indicates a good correlation among the pores. It is clear that the pore correlation of the felsic mineral lamina is best among all the kinds of laminae since.

Its curve is above the curves of other laminae when the distance is larger than 10 μm. Therefore, the macropores of the felsic mineral lamina present the largest aperture among all the kinds of laminae, and the correlation of the macropores is the highest. The average pore and throat radii of the clay mineral lamina are the smallest.

4.2.2. Effect of lamina type on mesopores

To investigate the effects of the lamina type on mesopore properties, twelve shales with different laminae from the GD12 and GD14 wells are used for the low-pressure N_2 and CO_2 adsorption experiments. Mineral identification of these samples was conducted using X-ray diffraction (XRD) analysis. Based on the mineral types and percentages, the samples are classified into the felsic mineral lamina, the carbonate mineral lamina, and the mixed mineral lamina. Low-pressure N_2 and CO_2 adsorption experiments are performed on these laminae to characterize their mesopore and micropore characteristics, respectively.

A comprehensive analysis of the curves in Fig. 11 reveals that the N_2 adsorption-desorption curves of these laminae in this study exhibit similarities. In the low-pressure region (P/P_0 < 0.4), the curves rise slowly with increasing relative pressure, indicating the presence of micropores. In the high-pressure region (P/P_0 > 0.8), the curves rise sharply, showing a downward concavity. Then, they continue to rise even as the relative pressure approaches the saturation vapor pressure ($P = P_0$), without leveling off, suggesting the development of multi-scale pores. In the intermediate pressure region (0.4 < P/P_0 < 0.8), the adsorption and desorption curves separate, forming a hysteresis loop, indicating the presence of a certain number of mesopores. Different types of laminae have varying mineral compositions, leading to differences in mesoporous characteristics.

For the felsic mineral laminae, their adsorption curves do not saturate as the relative pressure approaches 1 in Fig. 11(a), indicating the development of multi-scale pores and the presence of relatively large open pores or fractures. During nitrogen desorption, the increase in adsorption capacity in the medium-high pressure region is relatively slow, which possibly results from the connectivity of the pore structure. The desorption curves show a rapid initial decline followed by a slower decline, concave toward

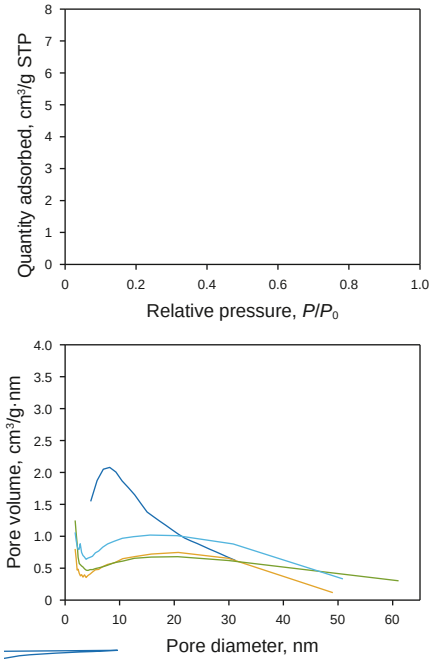

Fig. 11. The low-pressure N_2 adsorption curves and mesopore diameter distribution of four kinds of laminae. P and P_0 represent relative pressure and saturated vapor pressure, respectively. Felsic mineral lamina 1, 3852.56 m, GD12 well. Felsic mineral lamina 2, 3873.68 m, GD12 well. Felsic mineral lamina 3, 4137.78 m, GD14 well. Felsic mineral lamina 4, 4119.8 m, GD14 well. Carbonate mineral lamina 1, 3836.39 m, GD12 well. Carbonate mineral lamina 2, 3894.21 m, GD12 well. Carbonate mineral lamina 3, 4087.15 m, GD14 well. Carbonate mineral lamina 4,4131.7m, GD14. Mixed mineral lamina 1, 4085.95 m, GD14 well. Mixed mineral lamina 2, 4117.26 m, GD14 well. Mixed mineral lamina 3, 4127.78 m, GD14 well. Mixed mineral lamina 4, 4143.61 m, GD14 well.

the horizontal axis ($P/P_0 > 0.8$). As the relative pressure decreases, the desorption curves in the medium-pressure region ($0.4 < P/P_0 < 0.8$) and the low-pressure region ($P/P_0 < 0.4$) steadily decline and coincide with the adsorption curve at $P/P_0 \approx 0.47$. The hysteresis loop indicates the presence of slit-shaped pores and narrow fracture pores.

For the carbonate mineral laminae, the overall variation trend of their curves is similar to that of felsic laminae in Fig. 11(b), but the adsorption capacity increases more significantly in the medium-high pressure region, due to better pore connectivity. Additionally, the adsorption curve of calcareous-dolomitic laminae shows a distinct inflection point at a relative pressure of around 0.5, possibly related to the filling of pores of specific sizes. The desorption curves exhibit a 'fast-slow-fast' stepwise decline in the range of $0.5 < P/P_0 < 1$, with a noticeable plateau, and coincide with the adsorption curves at $P/P_0 = 0.47$. The hysteresis loop reveals the presence of slit-shaped pores and narrow fracture pores. For the mixed mineral laminae, their curve characteristics are generally similar to the previous two types of laminae in Fig. 11(c), with the main difference being that the adsorption capacity in the medium-high pressure region is lower than that of the carbonate mineral laminae. The hysteresis loop uncovers the development of layered slit pores and narrow fracture pores.

A comparison of the mesoporous characteristics of these laminae reveals that carbonate mineral laminae have higher specific surface areas and total pore volumes, indicating relatively well-developed nanoporous storage spaces. According to the pore volume increment curves, the mesopore volume in felsic mineral laminae is mainly provided by the pores whose sizes are between 7 and 40 nm, while in carbonate mineral laminae, the pores from 3 to 30 nm occupy a large amount of the pore space. In the mixed laminae, their pore volume mostly comprises the pores with a size between 4 and 35 nm (Fig. 11(d)–(f)).

From the perspective of the mesopore size, the mesopores in the felsic mineral laminae are relatively uniform, predominantly consisting of larger mesopores. In contrast, carbonate mineral laminae exhibit more complex mesopores, including both smaller and larger mesopores. The pore structures of the mixed mineral laminae consist of the smallest mesopores. These differences arise from the mineral crystal structure and arrangement, and the diagenetic changes of different minerals. Felsic minerals typically have a more stable crystal structure, which leads to more interparticle pores. On the other hand, carbonate minerals are prone to undergo dissolution and recrystallization during diagenesis, causing the formation of a complex pore network. In summary, three laminae with different mineral compositions of the Kong 2 Member exhibit significant heterogeneity. The pore types, pore size distributions, and porosity levels exhibit notable variations among the different laminae. Specifically, the mesopores in the felsic mineral laminae and carbonate mineral laminae are generally larger compared to those in mixed mineral laminae.

4.2.3. Effect of lamina type on micropores

The relationship between the adsorption amount and relative pressure can be used to derive the CO_2 adsorption curves, which qualitatively characterize the microporous structures of different laminae. As displayed in Fig. 12, the CO_2 adsorption curves of the selected lamina samples in this study exhibit similar shapes. The adsorption amount increases gradually with rising relative pressure and then slows, indicating the occurrence of micropores. The maximum CO_2 adsorption amounts vary among different lamina types, reflecting differences in the degree of microporous development. Among them, the carbonate mineral laminae show the highest adsorption amount, uncovering a relatively better pore structure. From Fig. 12(d)–(f), it can be observed that the microporous volumes of the three types of laminae are mainly concentrated in the range of between 0.4 nm and 0.8 nm, with fewer micropores developed in the 0.6–0.8 nm range. The carbonate mineral laminae, however, exhibit a peak in the 0.8–1 nm range. The CO_2 adsorption curves of felsic mineral laminae show a relatively gentle upward trend, which may be related to the crystal structure and arrangement of felsic minerals. Among the four felsic mineral laminae, the overall trend of the curvesis similar, but the adsorption amounts differ, indicating that even within the

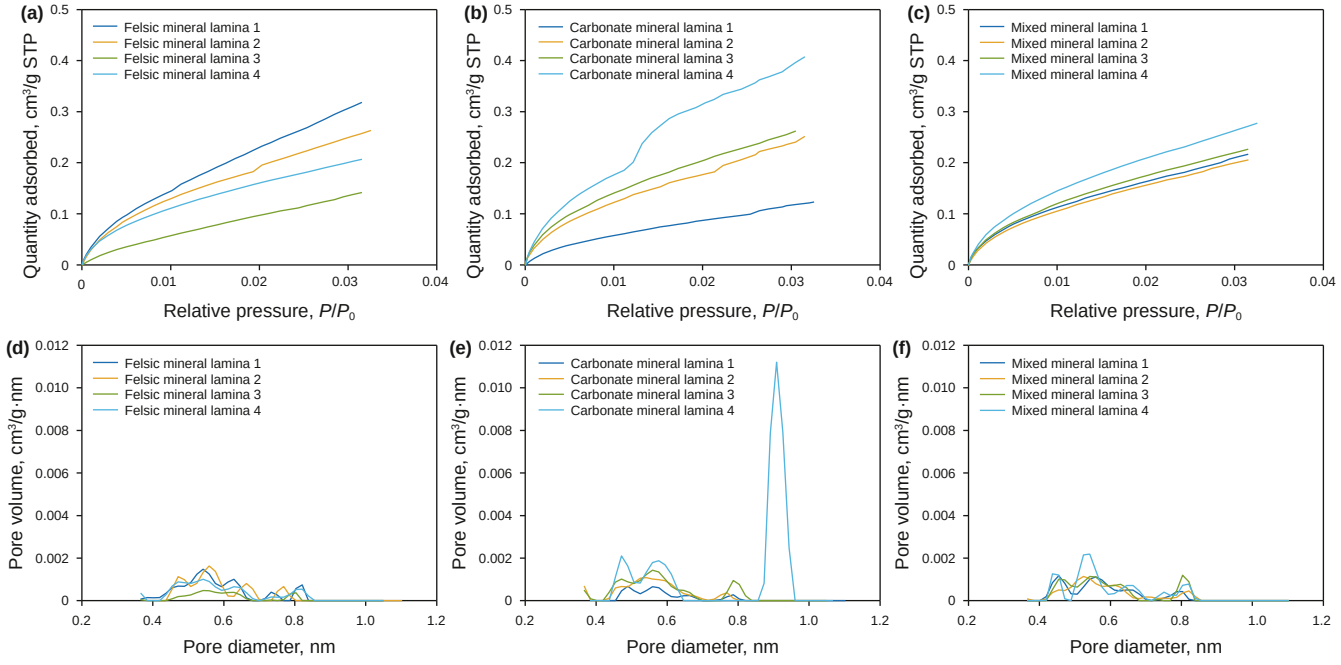

Fig. 12. The low-pressure CO_2 adsorption curves and micropore diameter distribution of the felsic mineral lamina, the carbonate mineral lamina, and the mixed mineral lamina. Others are the same as Fig. 11.

same type of lamina, pore structures can vary depending on depth and reservoir quality. Compared to the felsic mineral laminae, the carbonate mineral laminae exhibit similar curve characteristics, with a key difference being that their adsorption amount is the highest among the three types of laminae. The adsorption curve of the carbonate mineral lamina 4 rises more rapidly, revealing the presence of relatively larger pores. In contrast to the first two types of laminae, the curves of the mixed laminae show a higher overlap and greater uniformity. While their overall trend aligns with the first two types, their adsorption amount is comparatively the lowest among the three types of laminae. The carbonate mineral laminae samples exhibit the highest specific surface area and total pore volume, indicating the occurrence of the most developed micropores. From the pore volume increment curves in Fig. 12(d)–(f), it can be observed that the peaks of the carbonate mineral laminae are relatively regular and exhibit a multi-peak feature, with peaks at 0.45, 0.6, and 0.8 nm. The felsic mineral laminae show relatively well-developed pores in the range of 0.4–0.6 nm. In contrast to the first two types of laminae, the mixed mineral laminae have smaller micropore sizes.

All in all, the carbonate mineral lamina consists of some largest micropores, followed by the felsic mineral laminae, with the mixed laminae mainly containing numerous tiny micropores. In contrast, the felsic mineral lamina consists of much larger mesopores, while the carbonate mineral lamina comprises the smallest mesopores.

4.2.4. Effect of lamina and laminaset types on permeability

Apart from the pore-system properties of laminae, the effects of the lamina type and laminaset type on their permeability are also investigated. The digital models of the laminasets are constructed by integrating the digital models of two kinds of laminae. For example, the digital model of the felsic-mineral-clay-mineral laminaset is fused with the models of the felsic mineral lamina and clay mineral lamina. The permeability of the digital models is computed by the aforementioned pore-network modeling method. More details can be found in our previously published article (Wu et al., 2023). The simulated permeability of the digital models is demonstrated in Fig. 13. The felsic mineral lamina exhibits the best permeability among the four kinds of laminae due to the highest connected porosity and largest pore radius. The permeability of the carbonate mineral lamina is much worse than the felsic mineral lamina since the connected porosity of the former is smaller than the latter. Also, the pores of the carbonate mineral lamina consist of plenty of smaller pores than the latter. The permeability of the mixed mineral and clay mineral laminae is very small. Moreover, the permeability of the clay mineral lamina is the lowest because its average pore and throat radii and coordination number are the smallest. Furthermore, the permeability of the three laminates is compared in Fig. 13(b). Thanks to the connected porosity and pore aperture of the excellent permeability of the felsic mineral lamina, the permeability of the felsic-mineral-clay-mineral laminaset is the best, while that of the mixed-mineral-clay-mineral laminaset is the worst. Besides, the permeability of all the laminasets is smaller than that of the single felsic mineral lamina due to the addition of tiny pores from the clay mineral lamina into the laminasets. Nevertheless, it is impossible that one certain shale reservoir only includes the felsic mineral lamina (Fig. 7). The felsic mineral lamina is always followed by the clay mineral lamina due to the sedimentary rules. Therefore, more felsic mineral laminae improve the permeability of a shale reservoir.

4.3. Lamina-scale fracture propagation and brittleness evaluation

Based on the AMICS technique, 2D mineral distributions of four types of laminae are obtained. According to the frequency of the laminae and laminasets, the following models comprising clay mineral lamina and other laminae are designed. Such a design aims to control the lamina variables and better evaluate the main impact factors during simulations. By combining two types of laminae, the felsic-mineral-clay-mineral laminaset (FM-ClMLs) (Fig. 14(a)), the carbonate-mineral-clay-mineral laminaset (CaM-ClMLs) (Fig. 14(g)), and the mixed-mineral-clay-mineral laminaset model (MM-ClMLs) (Fig. 14(m)) are constructed. The width and height of these models are 66 μm and 132 μm, respectively. To investigate the effect of laminae and laminaset type on the frackability of shale, finite element methods were employed to conduct uniaxial compression simulations on three groups of different digital models of three laminasets types along the vertical direction. During the simulations, the lower boundaries of the model are fixed, and displacement loading is applied along the longitudinal direction of the model at a loading rate of 1.32×10^{-3} μm each step. The homogeneity index is set to 4, and the friction angle is set to 35° in all the models. Apart from the differences in the mineral compositions of the models, the loading conditions and mineral parameter settings are identical across all the models. The mechanical parameters of the different minerals are listed in Table 1, and these parameters are set according to the previous nano-scratch experiment of all the minerals (Cao et al., 2025). The

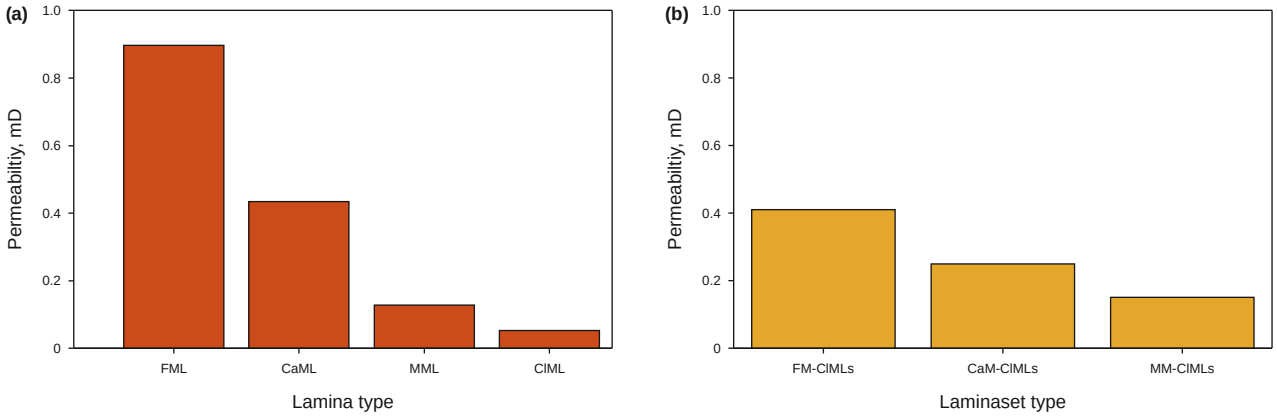

Fig. 13. The effects of lamina and laminaset types on the permeability of the shales. FML, CaML, MML, and ClML represent the felsic mineral lamina, carbonate mineral lamina, mixed mineral lamina, and clay mineral lamina, respectively. FM-ClMLs, CaM-ClMLs, and MM-ClMLs denote the felsic-mineral-clay-mineral laminaset, carbonate-mineral-clay-mineral laminaset, and mixed-mineral-clay-mineral laminaset, respectively.

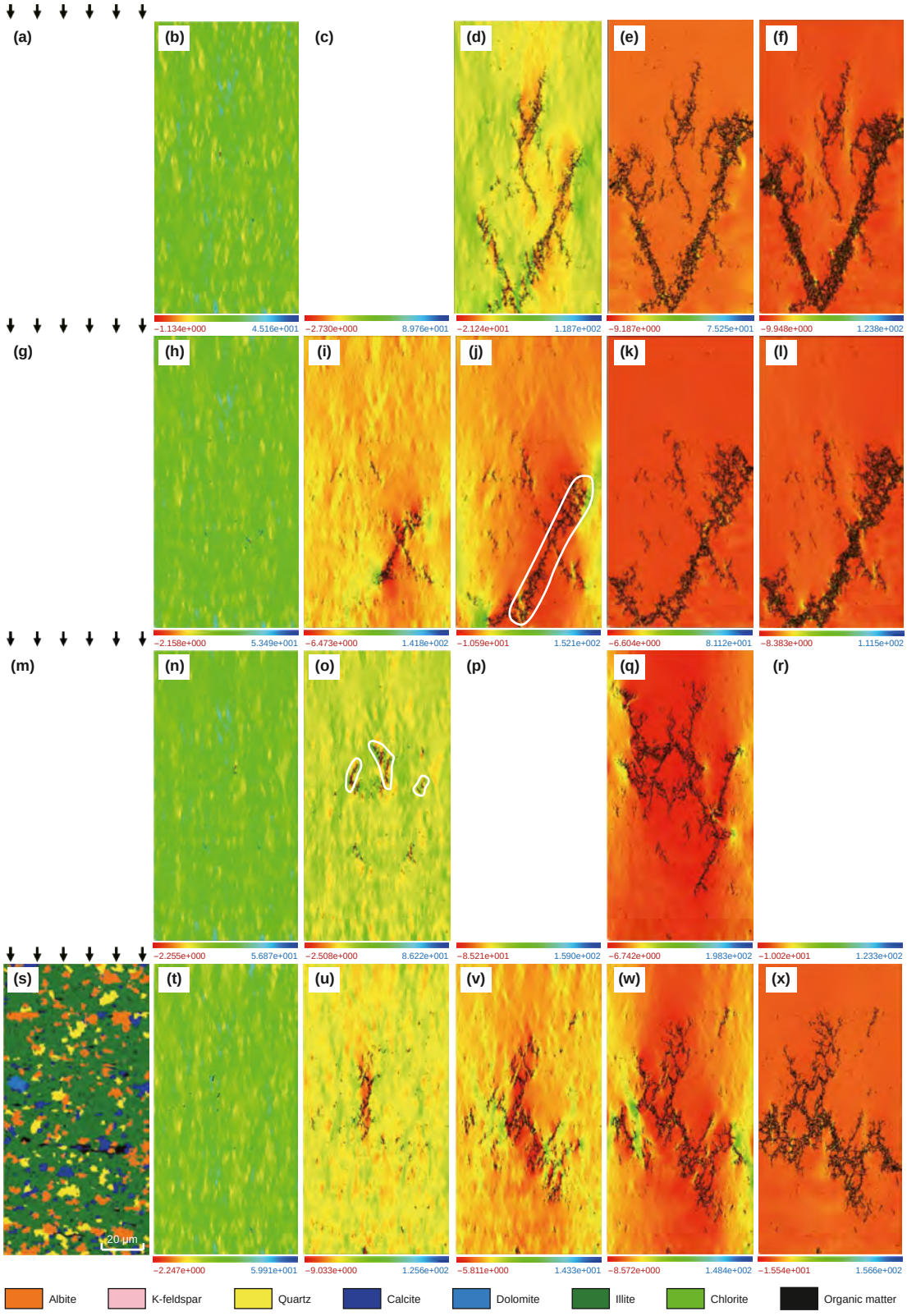

Fig. 14. Mineral compositions and maximum principal stress distribution of the felsic-mineral-clay-mineral laminaset (FM-ClMLs), the carbonate-mineral-clay-mineral laminaset (CaM-ClMLs), and the mixed-mineral-clay-mineral laminaset (MM-ClMLs). The arrows indicate the direction of the applied force. The white ellipses highlight the key regions discussed in the text. **(a)**, **(g)**, and **(m)** represent the mineral compositions of the FM-ClMLs model, CaM-ClMLs model, and MM-ClMLs model, respectively. **(b)** shows the maximum principal stress distribution of the FM-ClMLs model near failure but undamaged. **(c)**, **(d)** and **(e)** manifest the maximum principal stress distribution at the early, middle, and late stages of failure for the FM-ClMLs model, respectively. (**f**) exhibits the maximum principal stress distribution after failure when displacement loading is applied to the FM-ClMLs model for a distance. **(h)** shows the maximum principal stress distribution of the CaM-ClMLs model near failure, but undamaged. **(i)**, **(j)**, and **(k)** demonstrate the maximum principal stress distribution at the early, middle, and late stages of failure for the CaM-ClMLs model, respectively. **(l)** displays the maximum principal stress distribution after failure when displacement loading is applied to the CaM-ClMLs model for a distance. **(n)** demonstrates the maximum principal stress distribution of the MM-ClMLs model

compression/tension coefficient represents the ratio of compressive strength to tensile strength.

4.3.1. Effect of lamina and laminaset type on fracture propagation

4.3.1.1. Felsic-mineral-clay-mineral laminaset. Based on the failure mode of the model, it can be observed that the model exhibits nearly complete brittle failure. By combining the maximum principal stress distribution (Fig. 14(b)–(f)) and the failure mode diagrams (Fig. 15(a)–(f)), the compression failure process of the FM-ClMLs model can be divided into 3 stages: elastic stage, failure stage, and stabilization stage.

During the elastic stage, the stress-strain relationship of the model is linear. Under external pressure, tensile stress concentrates at the interfaces between quartz and other softer minerals, particularly at the sharp edges of quartz near the boundaries with illite. However, the tensile strain threshold of the material is not reached, and the model shows minimal damage, with a very small number of acoustic emissions (AE). The AE technology is widely used in the study of dynamic damage processes within rocks. The basic principle is that high-frequency elastic waves are emitted when internal rock damage occurs, and by recording and analyzing these waves, the degree of rock damage can be determined (Lacidogna et al., 2019). As strain continues to increase, the damaged area gradually expands. At these boundaries between quartz or K-feldspar particles and illite within the felsic lamina, more obvious damage to the K-feldspar begins to appear (Fig. 15(a)). The reason is that K-feldspar is harder and more brittle than the clay mineral, and stress concentration tends to occur at its boundary with ductile minerals like illite. Moreover, its strength is lower than that of quartz, making it more prone to damage. This leads to the initiation of fractures at the junctions between the felsic mineral laminae and clay mineral laminae, as stress concentration often occurs at these interfaces where ductile minerals are adjacent to the brittle minerals.

During the failure stage, when the load reaches its peak, the fractures that are initiated during the elastic stage begin to expand and rapidly develop into larger fractures. Early, a compression stress concentration zone in the center of the model induces shear failure, forming fractures at an angle to the compression stress zone. These fractures then propagate along the maximum shear plane (Fig. 14(c)). Many fractures form at the boundaries between illite and albite, as well as between illite and quartz or K-feldspar. In the former mineral combination, fractures tend to extend into the interior of the albite, while fractures are more likely to extend along the boundaries between illite and K-feldspar (Fig. 15(c)). After two types of fractures form, they quickly propagate and connect, forming main fractures in the central and lower parts of the felsic mineral lamina with roughly "Y"-shaped or inverted "Y"-shaped structures that penetrate through the felsic lamina (Fig. 15(c)). The fractures continue to extend from the felsic mineral lamina to the clay mineral lamina. The main fractures on both sides of the model develop along two nearly symmetrical shear planes toward the ends of the model, eventually penetrating the clay lamina and forming a "V"-shaped main fracture at the bottom of the model where the two tails meet (Fig. 15(d)). The main fracture generated in the center of the model extends toward the ends, penetrating the clay lamina and forming nearly vertical, arc-shaped fractures (Fig. 15(d)). Finally, tensile stress concentration occurs on both sides, and the fractures continue to propagate. The fracture on the left side extends along its direction toward the clay mineral lamina, penetrating it and forming a complex fracture, while the fracture on the right side propagates toward the upper felsic lamina, ultimately forming a complex fracture network (Fig. 15(e)). During the stabilization stage, the main fracture network remains mostly unchanged with further load increases. Tensile stress concentration occurs at the sharp boundaries of the main fractures formed during the failure stage (Fig. 14(e) and (f)), causing small fractures to develop at the boundaries of the main fractures. Some minerals are also stripped away, leading to the widening of the fractures (Fig. 14(f)).

4.3.1.2. Carbonate-mineral-clay-mineral laminaset. Based on the maximum principal stress distribution (Fig. 14(h)–(l)) and failure mode (Fig. 15(g)–(l)), the compressive failure process of the CaM-ClMLs model can be divided into three stages: elastic stage, failure stage, and stabilization stage. In the elastic stage, the model behaves elastically. After strain accumulates to a certain extent before the model starts showing minor damage. However, this does not affect the overall stress-strain relationship, which remains linear. Toward the end of this stage, noticeable damage begins to appear in the carbonate lamina, primarily concentrated in the calcite at the interface between the carbonate mineral lamina and clay mineral lamina, shown in the white box of Fig. 15(g).

In the early part of the elastic stage, a microfracture in the lower part of the carbonate lamina develops into an "X"-shaped main fracture. The areas above and below the fracture experience compressive stress, while tensile stress concentrates at the lower-left and upper-right ends of the main fracture (Fig. 14(i)). The fracture propagates in these two directions, ultimately penetrating the clay lamina above and below the main fracture, forming an inclined main fracture, exhibited in the white circle of Fig. 14(j). In the left lower part of the clay lamina, tensile stress concentration occurs at the left side of the main fracture, and the main fracture then connects with a fracture above it, continuing to extend upward until the fracture stops at the left boundary of the model (Fig. 15(k)). At the right upper end of the main fracture, a complex and dense network of fractures develops. After the failure stage, the fractures stabilize. Finally, the CaM-ClMLs model exhibits a situation similar to the FM-ClMLs model, where local tensile stress concentrations cause minor damage, leading to the detachment of minerals and widening of the main fracture (Fig. 14(l)).

4.3.1.3. Mixed-mineral-clay-mineral laminaset. In the MM-ClMLs model, the proportions of felsic and carbonate minerals in the laminae are approximately equal. The failure of the MM-ClMLs model exhibits distinct brittle characteristics. Based on the maximum principal stress distribution (Fig. 14(n)–(r)) and failure mode (Fig. 15(m)–(r)) of the MM-ClMLs model, the compressive failure process is also divided into three stages: elastic stage, failure stage, and stabilization stage. Similar to the FM-ClMLs and CaM-ClMLs models, the stress-strain behavior in the elastic stage is linear. At the early stage, there is no significant damage. As the stage progresses, minor damage begins to appear in the mixed mineral lamina, mainly in calcite adjacent to weak minerals or next to stiff minerals (Fig. 15(m)). Three longitudinal main fractures develop in the mixed mineral lamina in the middle of the model (Fig. 14(o)). After the left and middle main fractures intersect, fracture propagation is hindered by a quartz particle. At this point, compressive stress zones appear above and below the intersection area of the two main fractures, while tensile stress concentrations develop on both sides of the two main fractures

near failure but undamaged. **(o)**, **(p)**, and **(q)** exhibit the maximum principal stress distribution at the early, middle, and late stages of failure for the MM-ClMLs model, respectively. (r) shows the maximum principal stress distribution after failure when displacement loading is applied to the MM-ClMLs model for a distance.

(Fig. 14(p)). Fractures propagate along the paths with energy being released from the lower-left and upper-left sides of the left main fracture, and the upper-right and lower-right sides of the middle main fracture. Fractures on the left-upper and right-upper sides penetrate the clay lamina, while the fractures on the lower-right side penetrate downward through the clay lamina and connect with fractures formed in the middle-lower part of the mixed mineral lamina. A fracture region containing three parallel fractures forms at the lower-left side of the left main fracture (Fig. 15(p)). The right main fracture also extends longitudinally to some degree. Subsequently, energy continues to be released at the fracture tips until the left and right main fractures extend to the boundaries of the model (Fig. 15(q)). At the stabilization stage, the fracture shape does not change, and the main fractures widen slightly due to local stress concentration (Fig. 14(r)).

qJ9A11u1fAS1ajI69Ac9A1TdlH_qSI051s_XTiJ0Awk0keY-62MLsbSI051s_"1HXTiJ0thWXTiJTdlHYYkSIHAw1t9XTiJ9TiJTdlH_qSI051s_XTiJ0Awkwzl YAv

4.3.2. Effect of lamina type on brittleness and fracture fraction

Table 2 compares the mechanical properties and brittleness of three kinds of laminaset. When calculating the brittleness index according to Eqs. (10)–(12), the Young's modulus and Poisson's ratio results derived from the pure felsic mineral and pure clay mineral models are adopted to represent the maximum and minimum values within the reservoir. When the ultimate stress state is reached, the rock would fracture suddenly, and the fractures would propagate rapidly. In contrast, under low elastic modulus, rocks exhibit more plastic behavior, with larger plastic deformation and slip occurring within the rock before failure, and fractures would develop gradually. Rocks with low brittleness usually require more energy to fail. Therefore, a shale sample with high brittleness prefers to generate more fractures. Among these three models, the FM-ClMLs model has the highest Young's modulus and lowest Poisson's ratio, while the CaM-ClMLs model has the smallest Young's modulus and largest Poisson's ratio (Table 2). Moreover, the brittleness index of the FM-ClMLs model is the highest, followed by the MM-ClMLs model, and that of the CaM-ClMLs model is the lowest. Besides, the fracture area fraction of a model directly reflects the fluid passage area created when the rock fractures. Fractures with larger area fractions can provide channels for oil seepage and increase permeability, which helps improve production capacity. The fracture area fraction provides an intuitive measure of frackability. Among the three models, the FM-ClMLs model performs the highest fracture area ratio, followed by the MM-ClMLs model, and the CaM-ClMLs model has the lowest (Table 2). Therefore, the FM-ClMLs model has the highest frackability, followed by the MM-ClMLs model, and the CaM-ClMLs model has the lowest. This result is consistent with the conclusions drawn from the analysis of the brittleness.

Among all the minerals, the stiffness of calcite is stronger than that of albite and K-feldspar, and that of dolomite is the largest. However, the dolomite and calcite particles in the carbonate mineral laminae do not directly interconnect since carbonate mineral particles always link together via clay minerals, as manifested in Figs. 5 and 14. However, the quartz, albite, and K-feldspar particles in the felsic mineral laminae directly interconnect. As a result, the dolomite and calcite in the carbonate mineral laminae have poorer interconnectivity than that of the quartz, albite, and K-feldspar in the felsic mineral laminae. Therefore, both the mineral stiffness and the interconnectivity of mineral particles in a shale sample control its brittleness. Comparing Fig. 15(e), (k), and (q), the FM-ClMLs model shows two nearly symmetrical shear failure surfaces, while the CaM-ClMLs model displays a single shear failure surface, but with a lower inclination compared to the FM-ClMLs model. The overall brittleness and Young's modulus of the FM-ClMLs model are greater than those of the CaM-ClMLs model. The MM-ClMLs model does not exhibit obvious shear failure sur-

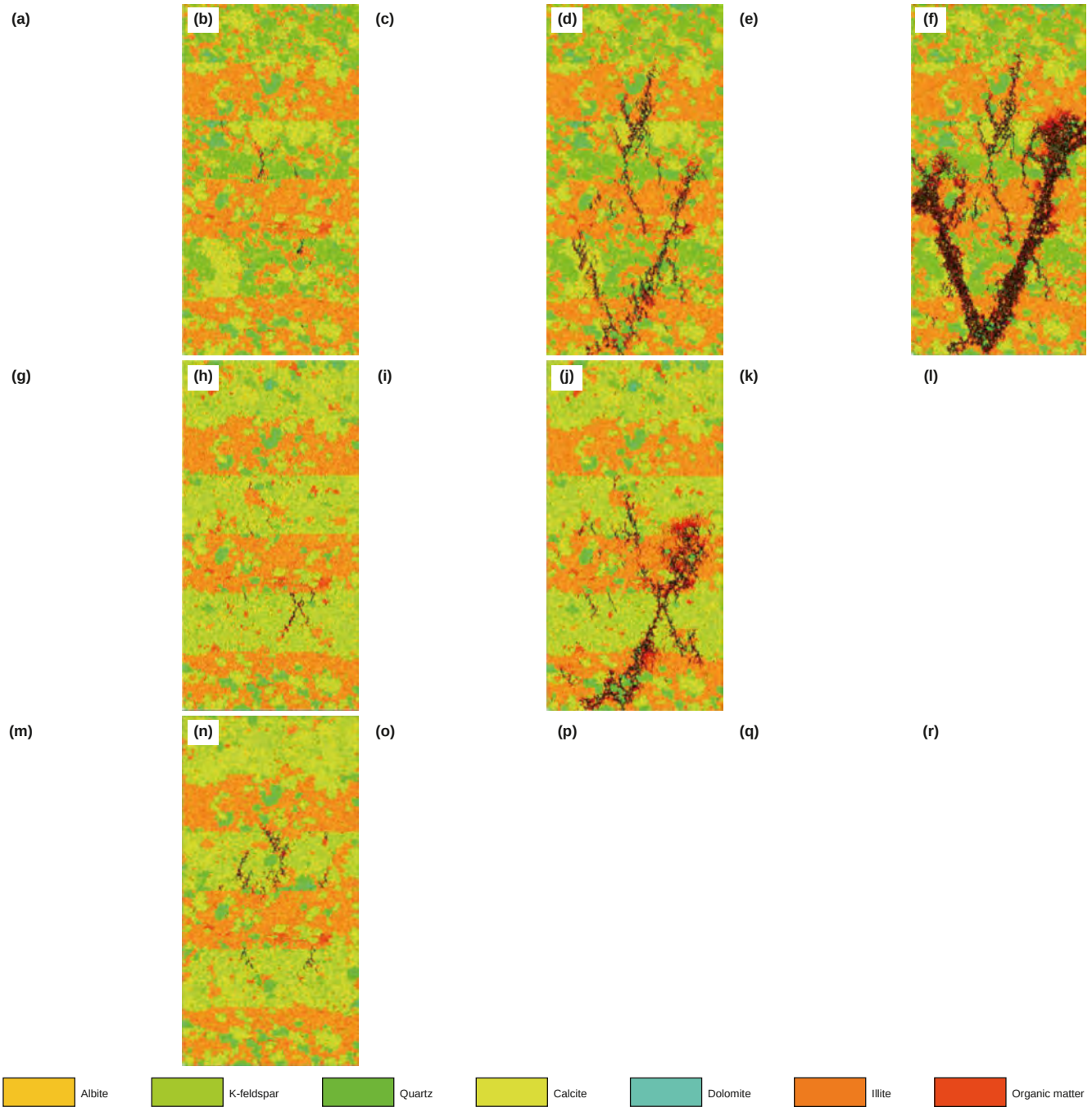

Fig. 15. Failure mode diagrams of the FM-ClMLs, CaM-ClMLs, and MM-ClMLs. White boxes highlight the initially generated microfractures. **(a)** shows the failure mode of the FM-ClMLs near failure, but undamaged. **(b)**, **(c)**, **(d)**, and **(e)** manifest the failure modes of the FM-ClMLs at the early, middle, and late stages of failure, and when failure is complete, respectively. **(f)** presents the failure mode after displacement loading. **(g)** reveals the failure mode of the CaM-ClMLs model near failure, but undamaged. **(h)**, **(i)**, **(j)**, and **(k)** exhibit the failure modes of the CaM-ClMLs at the early, middle, and late stages of failure, and when failure is complete, respectively. **(l)** demonstrates the failure mode after displacement loading. (**m**) displays the failure mode of the MM-ClMLs near failure but undamaged. **(n)**, **(o)**, **(p)**, and **(q)** represent the failure modes of the MM-ClMLs model at the early, middle, and late stages of failure, and when failure is complete, respectively. **(r)** shows the failure mode after displacement loading.

Table 2
Mechanical properties and brittleness of three kinds of laminasets.

Models	Young's modulus, MPa	Poisson's ratio	Brittleness index, %	Fracture area fraction, %
FM-ClMLs	58,261–59,182	0.153–0.155	59.94–66.03	13.99–15.29
CaM-ClMLs	57,121–58,572	0.164–0.166	38.79–41.04	10.40–11.07
MM-ClMLs	57,967–64,244	0.160–0.163	50.27–57.61	10.16–12.58

*FM-ClMLs, CaM-ClMLs, and MM-ClMLs represent felsic-mineral-clay-mineral laminaset, carbonate-mineral-clay-mineral laminaset, and mixed-mineral-clay-mineral laminaset, respectively.

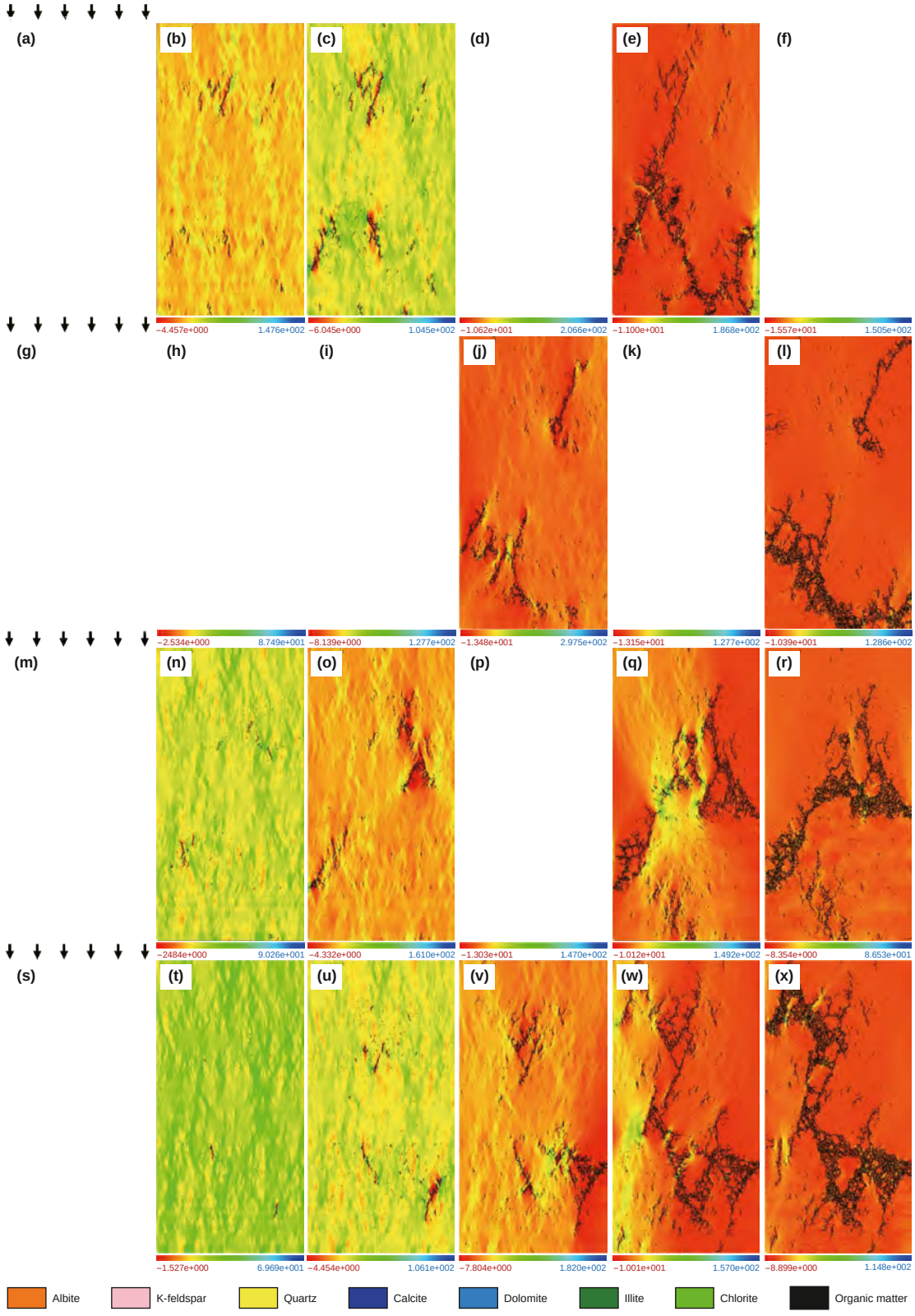

Fig. 16. Mineral compositions and maximum principal stress distribution in FM-ClMLs 1–4 with increasing felsic mineral lamina thickness. FM-ClMLs represents the felsic-mineral-clay-mineral laminaset. The arrows indicate the direction of the applied force. The white boxes highlight the initially generated microfractures. Others are the same as Fig. 14, but for FM-ClMLs 1–4.

Fig. 17. Failure modes of FM-ClMLs 1–4 with increasing felsic mineral lamina thickness. The white boxes highlight the initially generated microfractures. Others are the same as Fig. 15, but for FM-ClMLs 1–4.

compression simulation tests are conducted on three groups of four different models. The simulation conditions and parameters used in this simulation are identical to those in the previous simulation.

(1) Felsic-mineral-clay-mineral laminaset 1 (FM-ClMLs 1)

Under vertical compressive stress, microfractures first initiate in albite and K-feldspar within the felsic lamina, specifically at their contact interfaces with illite (Fig. 17(a)). These microfractures are induced by localized compressive stress concentration and primarily develop in the longitudinal direction (Fig. 16(b)). Under the influence of compressive stress, microfractures propagate at a certain inclination, penetrating the felsic lamina (Figs. 16(c) and 17(b)). The two fractures generated in the lower felsic lamina continue to extend along their original angles, gradually penetrating the middle and lower clay laminae (Fig. 17(c)). Among these two fractures, tensile stress concentration appears at both ends of the right-side fracture (Fig. 17(d)). Under tensile stress, the two fractures connect to form a "Z"-shaped main fracture, while one end of the right-side fracture bifurcates and extends laterally towards the model boundary (Fig. 16(e)). Meanwhile, the fracture formed in the upper felsic lamina propagates downward but does not connect with the main fracture below (Fig. 17(e)). The right-side fracture extends to the model boundary, at which point the model fails. After failure, when an additional displacement load is applied, the primary fracture in the lower part of the model exhibits slight widening, but its overall morphology remains unchanged.

(2) Felsic-mineral-clay-mineral laminaset 2 (FM-ClMLs 2)

As the model approaches failure, significant compressive stress concentration is observed in both felsic laminae. Under compressive stress, microfractures initially form within albite in the felsic lamina (Fig. 16(g) and (h), white box). Similar to the FM-ClMLs 1, these microfractures propagate along an inclined direction, penetrating the felsic lamina (Fig. 17(h)). One fracture in the upper felsic lamina and two fractures in the lower felsic lamina attempt to extend into the middle clay lamina but encounter dolomite and quartz (Fig. 17(i)). These stiff minerals obstruct further fracture propagation in the central clay lamina. The accumulated energy during loading is then released in the lower felsic lamina and the bottom clay lamina of the model. Under tensile stress, a horizontally oriented fracture zone emerges in the lower felsic and clay laminae, while the fracture in the upper felsic lamina propagates into the upper clay lamina until it reaches the model boundary (Fig. 16(j) and (k)). The final fracture morphology of FM-ClMLs 2 at failure is shown in Fig. 17(k). After failure, when an additional displacement load is applied, the fractures in the lower part of the model exhibit slight widening, while the upper fractures remain largely unchanged.

(3) Felsic-mineral-clay-mineral laminaset 3 (FM-ClMLs 3)

As the model approaches failure, multiple compressive stress concentration regions appear in both felsic laminae, forming strip-like patterns that are vertically distributed within the felsic laminae (Fig. 16(n)). This phenomenon is also observed in the FM-ClMLs 2. Some of these compressive stress concentration regions in the two felsic laminae begin to experience localized failure, generating multiple microfractures. In the upper felsic lamina, compressive stress concentration occurs above and below the microfractures. These microfractures start to extend at an inclined angle relative to the compressive stress zone, forming a "λ"-shaped shear failure region (Fig. 17(o)). Fractures generated in the lower felsic lamina penetrate the lamina and begin propagating obliquely upward. The two main fractures formed in the upper and lower regions gradually extend into the clay lamina while maintaining their basic morphology. A tensile stress concentration zone appears between the fracture tips (Fig. 17(p)). Under tensile stress, illite in the stress concentration zone undergoes tensile failure, forming a complex fracture network connecting the two main fractures (Fig. 17(q)). Meanwhile, the right end of the "λ"-shaped fracture extends toward the model boundary under tensile stress (Figs. 16(p) and 17(q)), completing the process that ultimately results in the failure. After failure, when additional displacement load is applied, the fracture morphology remains largely unchanged (Fig. 17(r)).

(4) Felsic-mineral-clay-mineral laminaset 4 (FM-ClMLs 4)

During failure, fractures initially emerge in albite and K-feldspar at the interface between the felsic and clay laminae (Fig. 17(s), white box). Under compressive stress, three microfractures initiate at the lamina boundary and first extend into the felsic lamina (Fig. 17(t)). These three fractures penetrate the felsic lamina, with two of them forming a "V"-shaped shear failure region (Fig. 16(v)). The already previously formed fractures then propagate toward the upper and middle clay laminae. A localized tensile stress concentration zone appears in the central part of the model, where downward- and upward-propagating fractures converge. Simultaneously, the upper fracture extends upward through the clay lamina (Figs. 16(w) and 17(v)). At this stage, the model has not reached complete failure. A tensile stress concentration zone appears at the left fracture tip, leading to further lateral expansion and acting as the final trigger for failure (Fig. 17(w)). After failure, when an additional displacement load is applied, localized tensile stress concentration results in significant fracture widening (Figs. 16(x) and 17(x)). The thickness ratios of the felsic laminae in the four models, FM-ClMLs 1, FM-ClMLs 2, FM-ClMLs 3, and FM-ClMLs 4, are 1:1.5:2:2.5. As shown in the comparison of Young's modulus and brittleness (Table 3), when the shales are composed of felsic and clay mineral laminae, the overall Young's modulus and brittleness of the models increase as the thickness of the felsic mineral lamina increases. Table 3 also indicates that the fracture area fraction increases with the thickening of the felsic lamina. Based on the trends observed in both brittleness and fracture area fraction, it can be concluded that the frackability of the models improves as the thickness of the felsic lamina increases.

By comparing Fig. 17(e), (k), (q), and (w), the following observations can be made. In the FM-ClMLs 1, fractures appear in both felsic laminae. The fracture generated in the upper felsic lamina tends to propagate longitudinally while its downward extension is hindered. The fracture in the lower felsic lamina initially extends longitudinally, but upon entering the clay lamina, it shifts to lateral propagation. As a result, the fractures in the upper and lower parts of the model remain unconnected. In FM-ClMLs 3, the fracture in the upper felsic lamina tends to extend downward, whereas the fracture in the lower felsic lamina propagates upward. When these two fractures reach the clay lamina, they form a lateral failure zone in the middle of the model, effectively connecting the two main fractures. In FM-ClMLs 4, fractures in both the upper and lower felsic laminae propagate predominantly in the longitudinal direction, penetrating the clay laminae in the upper and middle regions of the model. The fractures formed in the two felsic laminae are fully connected.within the model, but its vertical growth and width are significantly limited. Moreover, it does not connect with the main fracture in the lower region. In FM-ClMLs 2, the fracture in the upper felsic lamina primarily propagates

Table 3
Mechanical properties and brittleness of four kinds of laminasets.

Models	Young's modulus, MPa	Poisson's ratio	Brittleness index, %	Fracture area fraction, %
FM-ClMLs 1	50,916–53,854	0.162–0.166	29.55–31.51	7.89–9.75
FM-ClMLs 2	52,021–53,354	0.160–0.164	31.90–38.15	8.71–11.10
FM-ClMLs 3	54,228–56,012	0.161–0.163	39.00–44.46	9.44–13.24
FM-ClMLs 4	57,325–58,463	0.156–0.159	52.65–56.97	11.66–15.27

*FM-ClMLs represents the felsic-mineral-clay-mineral laminaset.

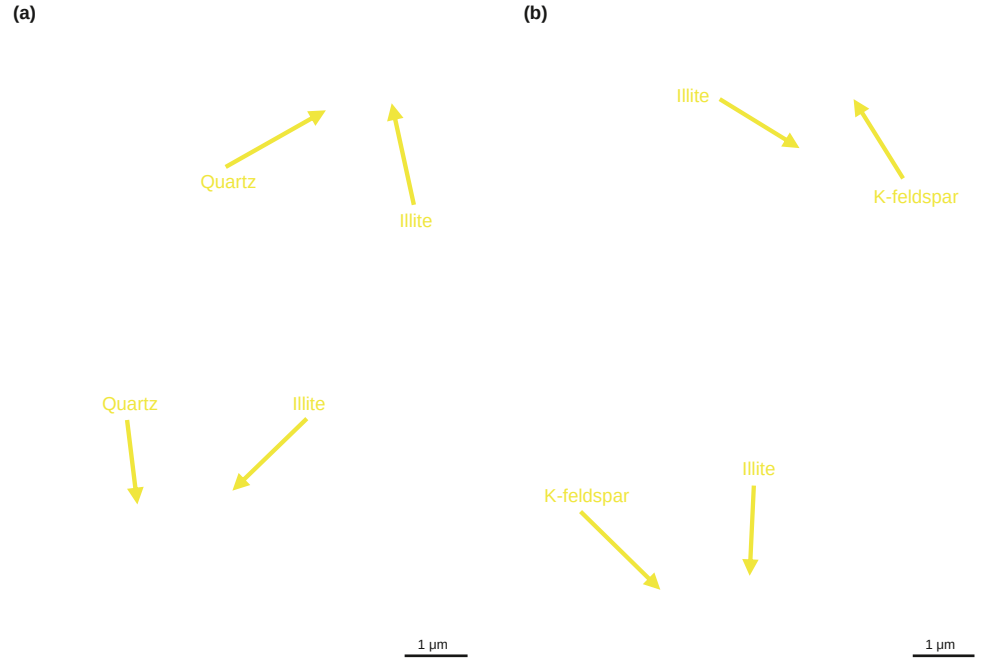

Fig. 18. Fracture initiation and propagation characteristics based on SEM experiments. (**a**) 3049.36 m, G108-8 well. (**b**) 2981.68 m, G108-8 well.

upward. In terms of the interface elements or interface weakening, there exists a narrow interface between the two kinds of minerals. Shales are fine-grained sedimentary rocks. The interfaces between illite and brittle minerals in shales are extremely thin and their thicknesses are less than several tens of nanometers (Fig. 4). If the nanometer interfaces are considered in the simulation, the sizes of the models would increase to about one billion grids/pixels. As such, it would be extremely difficult to simulate the fracture propagation on such large models with one billion pixels. In the future, when supercomputing and clustering are available and FEM parallel algorithms are developed, it may be possible to implement simulations considering the interface weakening. However, the nanometer interfaces would only have a minor effect on fracture propagation and would hardly affect the evaluation results of shale brittleness (Ju et al., 2022).

To validate that the preferred fracture initiation occurs at the boundaries between the ductile and brittle minerals, such as illite and quartz or K-feldspar, Fig. 18 displays the experimental fracture initiation characteristics. Fractures usually form at the boundaries between illite and quartz, or illite and K-feldspar. Therefore, the fracture initiation simulation is in good agreement with the fracture generation experiment and the findings in other studies (He et al., 2019; Hoek and Martin, 2014).

In terms of the limitations of the methods that are applied in this paper, the characterized sample size of the FIB-SEM experiment is at present not too large, only a few square millimeters, since the current instrument cannot satisfy the requirements for large-view imaging with an ultra-high resolution. Moreover, the mineral type cannot be quantitatively distinguished in the FIB-SEM images alone since the grayscale values of quartz, feldspar, and calcite are too similar to be segregated. As to the gas adsorption experiments, the N_2 and CO_2 methods are used for characterizing the mesopores and micropores, respectively. It is difficult to characterize all the pores by using only a single method. Besides, the simulated grid size of the FEM method is usually smaller than one hundred million pixels.

In the studied formation, Ek_2 in the Cangdong Sag, Bohai Bay Basin, the lamina types, mineral combinations, and diagenetic history are specific in this area, which are different from other shale formations such as the Shahejie Formation in the Jiyang Depression, Bohai Bay Basin, or the Yangchang Formation in the Ordos Basin. The shales in the Shahejie Formation are composed of micritic calcite lamina, sparry calcite lamina, mixed mineral lamina, clay mineral lamina, organic matter lamina, dolomite lamina, and anhydrite lamina due to their specific lacustrine settings (Liang et al., 2023). Diagenesis has a great effect on the mineral content and brittleness of shales in the Shahejie Formation since calcite and dolomite exist in different forms from those of Ek_2 in the Cangdong Sag. The shales in the Yangchang Formation consist of tuff-rich lamina, organic-rich lamina, felsic mineral lamina, and clay mineral lamina, which are different from those reported in this study (Cao et al., 2024; Xi et al., 2020). Therefore, the effects of lamina on the petrophysical and mechanical properties in different study areas would be distinct. However, the comprehensive

lamina-scale experimental characterization and numerical simulation methods and workflow proposed in this paper can be used for the evaluation of the petrophysical and mechanical properties of other shale formations.

5. Conclusions

This study proposes a novel technique combining experimental and numerical methods to characterize the petrophysical properties and brittleness of shales at the lamina scale. The laminated shales of the Second Member of the Kongdian Formation of the

from the second member of Kongdian Formation in the Cangdong Sag, Bohai Bay Basin, East China. Petrol. Explor. Dev. 49 (5), 943–954. https://doi.org/10.1016/S1876-3804(22)60334-3.
Fan, Y., 2023. Storage Capacity of Shale Oil Reservoirs in the Second Member of the Kongdian Formation in the Cangdong Sag, Bohai Bay Basin. China University of Petroleum, Dissertation (East China).
Ghanizadeh, A., Amann-Hildenbrand, A., Gasparik, M., et al., 2014. Experimental study of fluid transport processes in the matrix system of the European organic-rich shales: II. Posidonia Shale (Lower Toarcian, northern Germany). Int. J. Coal Geol. 123, 20–33. https://doi.org/10.1016/j.coal.2013.06.009.
Han, W., Zhao, X., Jin, F., et al., 2021. Sweet spot evaluation and exploration practice of lacustrine shale oil of the second member of Kongdian Formation in Cangdong Sag, Bohai Bay Basin. Petrol. Explor. Dev. 48 (4), 777–786. https://doi.org/10.1016/S1876-3804(21)60075-7.
He, J., Li, X., Yin, C., et al., 2019. Propagation and characterization of the micro cracks induced by hydraulic fracturing in shale. Energy 191, 116449. https://doi.org/10.1016/j.energy.2019.116449.
Hoek, E., Martin, C.D., 2014. Fracture initiation and propagation in intact rock—a review. J. Rock Mech. Geotech. Eng. 6 (4), 287–300. https://doi.org/10.1016/j.jrmge.2014.06.001.
Hu, Q., Zhang, Y., Meng, X., et al., 2017. Characterization of micro-nano pore networks in shale oil reservoirs of Paleogene Shahejie Formation in Dongying Sag of Bohai Bay Basin, East China. Pet. Explor 44 (5), 720–730. https://doi.org/10.1016/S1876-3804(17)30083-6.
Iqbal, M.A., Rezaee, R., Smith, G., et al., 2021. Shale lithofacies controls on porosity and pore structure: An example from Ordovician Goldwyer Formation, Canning Basin, Western Australia. J. Nat. Gas Sci. Eng. 89, 103888. https://doi.org/10.1016/j.jngse.2021.103888.
Jin, X., Li, G., Meng, S., et al., 2021. Microscale comprehensive evaluation of continental shale oil recoverability. Petrol. Explor. Dev. 48 (1), 222–232. https://doi.org/10.1016/S1876-3804(21)60021-6.
Jin, Z., Zhu, R., Liang, X., et al., 2021. Several issues worthy of attention in current lacustrine shale oil exploration and development. Petrol. Explor. Dev. 48 (6), 1471–1484. https://doi.org/10.1016/S1876-3804(21)60303-8.
Joekar-Niasar, V., Hassanizadeh, S.M., 2012. Analysis of fundamentals of two-phase flow in porous media using dynamic pore-network models: A review. Crit. Rev. Environ. Sci. Technol. 42 (18), 1895–1976. https://doi.org/10.1080/10643389.2011.574101.
Ju, M., Li, X., Li, X., et al., 2022. A review of the effects of weak interfaces on crack propagation in rock: From phenomenon to mechanism. Eng. Fract. Mech. 263, 108297. https://doi.org/10.1016/j.engfracmech.2022.108297, 2022.
Lacidogna, G., Piana, G., Carpinteri, A., 2019. Damage monitoring of three-point bending concrete specimens by acoustic emission and resonant frequency analysis. Eng. Fract. Mech. 210, 203–211. https://doi.org/10.1016/j.engfracmech.2018.06.034.
Lai, J., Wang, G., Fan, Z., et al., 2016. Research progress in brittleness index evaluation methods with logging data in unconventional oil and gas reservoirs. Pet. Sci. Bull. 3, 330–341.
Li, J., Yin, J., Zhang, Y., et al., 2015. A comparison of experimental methods for describing shale pore features: A case study in the Bohai Bay Basin of eastern China. Int. J. Coal Geol. 152, 39–49. https://doi.org/10.1016/j.coal.2015.10.009.
Liang, C., Cao, Y., Wu, J., et al., 2023. Water depth–terrigenous input dynamic equilibrium controls the Eocene lacustrine shale laminae records in Jiyang depression, Bohai Bay Basin, East China. Am. Assoc. Petrol. Geol. Bull. 107 (11), 1987–2016. https://doi.org/10.1306/07052321160.
Liu, B., Wang, H., Fu, X., et al., 2019. Lithofacies and depositional setting of a highly prospective lacustrine shale oil succession from the Upper Cretaceous Qingshankou Formation in the Gulong Sag, Northern Songliao Basin, Northeast China. Am. Assoc. Petrol. Geol. Bull. 103 (2), 405–432. https://doi.org/10.1306/08031817416.
Liu, X., Liang, Z., Meng, S., et al., 2022. Numerical simulation study of brittle rock materials from micro to macro scales using digital image processing and parallel computing. Appl. Sci. 12 (8). https://doi.org/10.3390/app12083864.
Liu, X., Meng, S., Liang, Z., et al., 2023. Microscale crack propagation in shale samples using focused ion beam scanning electron microscopy and three-dimensional numerical modeling. Pet. Sci. 20 (3), 1488–1512. https://doi.org/10.1016/j.petsci.2022.10.004.
Loucks, R.G., Reed, R.M., Ko, L.T., et al., 2021. Micropetrographic characterization of a siliciclastic-rich chalk; Upper Cretaceous Austin Chalk group along the onshore northern Gulf of Mexico, USA. Sediment. Geol. 412, 105821. https://doi.org/10.1016/j.sedgeo.2020.105821.
Loucks, R.G., Ruppel, S.C., 2007. Mississippian Barnett Shale: Lithofacies and depositional setting of a deep-water shale-gas succession in the Fort Worth Basin, Texas. Am. Assoc. Petrol. Geol. Bull. 91 (4), 579–601. https://doi.org/10.1306/11020606059.
Ma, L., Dowey, P.J., Rutter, E., et al., 2019. A novel upscaling procedure for characterising heterogeneous shale porosity from nanometer- to millimetre-scale in 3D. Energy 181, 1285–1297. https://doi.org/10.1016/j.energy.2019.06.011.
Ma, T., Liu, K., Su, X., et al., 2024. Investigation on the anisotropy of mesomechanical properties of shale rock using micro-indentation. Bull. Eng. Geol. 83 (1), 1–19. https://doi.org/10.1007/s10064-023-03510-y.
Mastalerz, M., Hampton, L.B., Drobniak, A., et al., 2017. Significance of analytical particle size in low-pressure N_2 and CO_2 adsorption of coal and shale. Int. J. Coal Geol. 178, 122–131. https://doi.org/10.1016/j.coal.2017.05.003Getrightsandcontent.
McMahon, T.P., Larson, T.E., Zhang, T., et al., 2024. Geologic characteristics, exploration and production progress of shale oil and gas in the United States: An overview. Petrol. Explor. Dev. 51 (4), 925–948. https://doi.org/10.1016/S1876-3804(24)60516-1.
Meng, S., Li, D., Liu, X., et al., 2023. Study on dynamic fracture growth mechanism of continental shale under compression failure. Gas Sci. Eng. 114, 204983. https://doi.org/10.1016/j.jgsce.2023.204983.
Nath, F., Mokhtari, M., 2018. Optical visualization of strain development and fracture propagation in laminated rocks. J. Pet. Sci. Eng. 167, 354–365. https://doi.org/10.1016/j.petrol.2018.04.020Getrightsandcontent.
Raeini, A.Q., Bijeljic, B., Blunt, M.J., 2017. Generalized network modeling: Network extraction as a coarse-scale discretization of the void space of porous media. Phys. Rev. E. 96 (1), 1–17. https://doi.org/10.1103/PhysRevE.96.013312.
Reed, R.M., Sivil, J.E., Sun, X., et al., 2019. Heterogeneity of Microscale Lithology and Pore Systems in an Upper Cretaceous Eagle Ford Group Horizontal Core, South Texas, vol. 8. U.S.A. GCAGS J., pp. 22–34
Rickman, R., Mullen, M., Petre, E., et al., 2008. A practical use of shale petrophysics for stimulation design optimization: All shale plays are not clones of the Barnett Shale. Proc. SPE Annu. Tech. Conf. Exhib. 2, 840–850. https://doi.org/10.2118/115258-MS.
Schieber, J., 1990. Significance of styles of epicontinental shale sedimentation in the Belt Basin, Mid-Proterozoic of Montana, U.S.A. Sediment. Geol. 69 (3–4), 297–312. https://doi.org/10.1016/0037-0738(90)90055-X.
Shi, Z., Qiu, Z., Dong, D., et al., 2018. Laminae characteristics of gas-bearing shale fine-grained sediment of the Silurian Longmaxi Formation of Well Wuxi 2 in Sichuan Basin, SW China. Petrol. Explor. Dev. 45 (2), 339–348. https://doi.org/10.1016/S1876-3804(18)30040-5.
Song, W., Liu, L., Sun, H., et al., 2021. Pore structure characterization and flow ability of shale oil reservoir based on digital cores. Pet. Reserv. Eval. Dev. 11 (4), 497–505.
Tang, C., Xu, Z., Xu, X., 1999. Application of analysis system RFPA2D of rock fracture process in researching moving rules of covering workface. J. Liaoning Tech. Univ. 18 (5), 456–458. CNKI:SUN:FXKY.0.1999-05-004 (in Chinese).
Tang, C., Zhao, W., 1997. RFPA2D system for rock failure process analysis. Chin. J. Rock Mech. Eng. 5 (16), 109–110.
Vernik, L., Nur, A., 1992. Ultrasonic velocity and anisotropy of hydrocarbon source rocks. Geophysics 57 (5), 727–735. https://doi.org/10.1190/1.1443286.
Wang, C., Zhang, B., Hu, Q., et al., 2019. Laminae characteristics and influence on shale gas reservoir quality of lower Silurian Longmaxi Formation in the Jiaoshiba area of the Sichuan Basin, China. Mar. Pet. Geol. 109, 839–851. https://doi.org/10.1016/j.marpetgeo.2019.06.022.
Wu, Y., An, S., Tahmasebi, P., et al., 2023. An end-to-end approach to predict physical properties of heterogeneous porous media: Coupling deep learning and physics-based features. Fuel 352, 128753. https://doi.org/10.1016/j.fuel.2023.128753.
Wu, Y., Tahmasebi, P., Yu, H., et al., 2020. Pore-scale 3D dynamic modeling and characterization of shale samples: Considering the effects of thermal maturation. J. Geophys. Res. Solid Earth 125 (1). https://doi.org/10.1029/2019JB018309 e2019JB018309.
Xi, K., Li, K., Cao, Y., et al., 2020. Laminae combination and shale oil enrichment patterns of Chang 73 sub-member organic-rich shales in the Triassic Yanchang Formation, Ordos Basin, NW China. Petrol. Explor. Dev. 47 (6), 1244–1255. https://doi.org/10.1016/S1876-3804(20)60142-8.
Xin, B., Zhao, X., Hao, F., et al., 2022. Laminae characteristics of lacustrine shales from the Paleogene Kongdian Formation in the Cangdong Sag, Bohai Bay Basin, China: Why do laminated shales have better reservoir physical properties? Int. J. Coal Geol. 260, 104056. https://doi.org/10.1016/j.coal.2022.104056.
Xu, S., Wen, J., Liu, K., et al., 2024. Brittle minerals, mechanical properties and fracability evaluation of shales. Adv. Geo-Energy Res. 14 (1), 8–11. https://doi.org/10.46690/ager.2024.10.03.
Xu, Z., Zheng, M., Liu, Z., et al., 2020. Petrophysical properties of deep Longmaxi Formation shales in the southern Sichuan Basin, SW China. Petrol. Explor. Dev. 47 (6), 1183–1193. https://doi.org/10.1016/S1876-3804(20)60128-3.
Yu, W., Sepehrnoori, K., Patzek, T.W., 2016. Modeling gas adsorption in marcellus shale with langmuir and bet isotherms. SPE J. 21 (2), 589–600. https://doi.org/10.2118/170801-PA.
Zhang, L., Lu, S., Jiang, S., et al., 2018. Effect of shale lithofacies on pore structure of the Wufeng-Longmaxi shale in southeast Chongqing, China. Energy Fuels 6603–6618. https://doi.org/10.1021/acs.energyfuels.8b00799.
Zhang, Y., Yang, Y., Martyushev, D., et al., 2025. Quantifying the effect of mineral compositions on the brittleness of shale using the finite element method. Pet. Res. 1–9. https://doi.org/10.1016/j.ptlrs.2025.08.001.
Zhao, L., Zhao, Y., Yan, D., et al., 2024. Integrated rock physics characterization of unconventional shale reservoir: A multidisciplinary perspective. Adv. Geo-Energy Res. 14 (2), 86–89. https://doi.org/10.46690/ager.2024.11.02.
Zhao, X., Pu, X., Zhou, L., et al., 2020a. Typical geological characteristics and exploration practices of lacustrine shale oil: A case study of the Kong-2

member strata of the Cangdong Sag in the Bohai Bay Basin. Mar. Pet. Geol. 113, 103999. https://doi.org/10.1016/j.marpetgeo.2019.08.027.
Zhao, X., Zhou, L., Pu, X., et al., 2019. Exploration breakthroughs and geological characteristics of continental shale oil: A case study of the Kongdian Formation in the Cangdong Sag, China. Mar. Pet. Geol. 102, 544–556. https://doi.org/10.1016/j.marpetgeo.2018.12.020.
Zhao, X., Zhou, L., Pu, X., et al., 2020b. Formation conditions and enrichment model of retained petroleum in lacustrine shale: A case study of the Paleogene in Huanghua Depression, Bohai Bay Basin, China. Petrol. Explor. Dev. 47 (5), 856–869. https://doi.org/10.1016/S1876-3804(20)60106-9.
Zhao, Y., Wang, Y., Wen, S., et al., 2025. In-situ experiments of dynamic microscopic reaction for CO_2-brine-carbonate system. Chem. Eng. J. 506 (11), 160251. https://doi.org/10.1016/j.cej.2025.160251.
Zhou, S., Zhang, D., Wang, H., et al., 2019. A modified BET equation to investigate supercritical methane adsorption mechanisms in shale. Mar. Pet. Geol. 105, 284–292. https://doi.org/10.1016/j.marpetgeo.2019.04.036.
Zhu, W., Tang, C., 2004. Micromechanical model for simulating the fracture process of rock. Rock Mech. Rock Eng. 37 (1), 25–56. https://doi.org/10.1007/s00603-003-0014-z.